

Uptake of CO₂ and Precipitation of Calcium Carbonate in Alkaline Solutions

Bettina Purgstaller

Institut für Angewandte Geowissenschaften
Technische Universität Graz

Betreuer:
Univ.-Prof.Dipl.-Min.Dr.rer.nat. Martin Dietzel

Mai 2013

STATUARY DECLARATION

I declare that I have authored this thesis independently, that I have not used other than the declared sources / resources, and that I have explicitly marked all material which has been quoted either literally or by content from the used sources

.....

.....

DATE

(SIGNATURE)

ACKNOWLEDGMENTS

First of all I would like to express my special thanks and appreciation to my advisor Prof. Martin Dietzel for his great support and the useful discussions, remarks and corrections during writing this thesis. Furthermore, I am also very grateful to Dr. Andrea Niedermayr, for her support in all questions concerning the experiments, subsequent calculations and discussions. I would like to say thanks to Dr. Albrecht Leis (Joanneum Research Graz) and Dr. Christine Latal for the oxygen isotopic and for the X-ray diffraction measurements, respectively. My gratitude goes also to Dr. Patrick Grunert and to Dr. Kurt Krenn (Karl Franzens University of Graz) for their support conducting scanning electron microscopy images and Raman spectroscopic analyses, respectively. I am grateful to Dr. Daniel Höllen for the ICP-MS analyzes as well as for his support concerning interpretations of the data. Special thanks to Andre Baldermann for his help in evaluating the XRD pattern and for helpful suggestions. Furthermore, thanks to Andrea Wolf, Maria Hierz and all the other colleagues for their great support in the laboratory. Last but not least I want to express my deepest gratitude to my family, who supported me during my entire study.

ABSTRACT

Calcium carbonates (CaCO_3) may be induced biogenically or inorganically in aqueous solutions. Biogenically induced CaCO_3 are of great significance in the marine environment, where organisms such as corals and calcareous plankton use CaCO_3 for their skeletons. Inorganically induced CaCO_3 occurs in marine and terrestrial systems e.g. where evaporates and sinter are formed. Nowadays, calcium carbonates are widely used in technical applications, e.g. as filler in paper industry. Precipitated CaCO_3 may also cause serious problems in heat exchangers or drainage systems. CaCO_3 can be induced by CO_2 degassing or absorption in aqueous solutions, depending on the pH and on the dissolved inorganic carbon content. Although, the formation conditions of CaCO_3 have been widely studied, significant gaps of knowledge exist for the reaction kinetics (CO_2 uptake and CaCO_3 precipitation) in alkaline solutions as well as for distinct CaCO_3 polymorph formations. Therefore, CO_2 uptake and CaCO_3 precipitation were experimentally studied by the diffusion of CO_2 through a membrane from an inner into an outer solution containing Ca^{2+} , Sr^{2+} and B (25°C). The pH of the outer solution was kept constant during the experiment at 8.30, 9.00, 10.00 11.00 or 11.50 by titration using a diluted NaOH solution. The evolution of the NaOH titration curve reflects parameters like the CO_2 uptake rate (\propto ACAR: aqueous CO_3^{2-} accumulation rate) and the overall precipitation rate of CaCO_3 (R_{CaCO_3}). Solid analyses identified the CaCO_3 polymorphs calcite (Cc), vaterite (Va) and aragonite (Ar). Ca and Va were precipitated at all pH values, whereas Ar was only present at $\text{pH} \geq 10.00$. At high pH, the ACAR is significantly higher compared to lower pH conditions, thus nucleation of CaCO_3 starts earlier. Interestingly, the amount of precipitated CaCO_3 was similar for all experiments for the given total experimental time. This can be explained by the significantly higher R_{CaCO_3} at low versus high pH, which correlates with a general decrease of $[\text{>CaHCO}_3^0]$ at the CaCO_3 surface. Thus, CaCO_3 quantification is controlled by combined effects of CO_3^{2-} accumulation and CaCO_3 precipitation kinetics. Furthermore, the coprecipitation of B and Sr^{2+} with CaCO_3 and the O-isotopic composition of CaCO_3 were investigated in the present study. The coprecipitation of B with CaCO_3 and the fractionation of $^{18}\text{O}^{16}\text{O}$ -isotopes depend on the pH value of the solution, whereas the incorporation of Sr^{2+} in the bulk CaCO_3 is determined by the proportion of aragonite.

KURZFASSUNG

Kalziumkarbonate (CaCO_3) können biogen oder anorganisch aus wässriger Lösung präzipitieren. Die biogene Abscheidung hat eine große Bedeutung im marinen System, da viele Organismen, wie beispielsweise Korallen oder kalkbildende Mikroorganismen, ihre Skelette aus CaCO_3 aufbauen. Anorganisch induzierte Abscheidungen von CaCO_3 treten im marinen und terrestrischen System z.B. bei der Bildung von Evaporiten und Sintern auf. Kalziumkarbonate werden heutzutage in vielen Bereichen technisch genutzt, wie z.B. als Füllstoff in der Papierindustrie. Jedoch kann abgeschiedenes CaCO_3 auch Probleme bereiten, beispielsweise in Wärmeaustausch- und Entwässerungssystemen. CaCO_3 kann in wässriger Lösung durch CO_2 Aufnahme oder Entgasung, je nach pH-Wert und Gehalt an gelöstem anorganischen Kohlenstoff, abgeschieden werden. Obwohl die Bildungsbedingungen von CaCO_3 umfangreich und seit langer Zeit untersucht werden, gibt es noch signifikante Wissenslücken insbesondere im Bereich der Reaktionskinetik (CO_2 Aufnahme und CaCO_3 Abscheidung) in alkalischen Lösungen und der spezifischen Bildung von CaCO_3 Polymorphen. Zu diesem Zweck ist die CO_2 Aufnahme und die Ausfällung von CaCO_3 experimentell untersucht worden, indem CO_2 von einer inneren Lösung durch eine Membran in eine äußere Ca^{2+} -, Sr^{2+} - und B- haltige Lösung diffundiert. Der pH-Wert der äußeren Lösung wurde während des gesamten Experiments bei pH 8.30, 9.00, 10.00, 11.00 oder 11.50 konstant gehalten durch die Titration einer verdünnten NaOH Lösung. Die Entwicklung der NaOH Titrationskurve ermöglicht die Bestimmung der CO_2 Aufnahme rate (\propto ACAR: CO_3^{2-} Akkumulationsrate in der Lösung,) und der CaCO_3 Abscheidungsrate (R_{CaCO_3}). Durch Analysen der resultierenden Festkörper wurden die CaCO_3 Modifikationen Calcit (Cc), Vaterit (Va) und Aragonit (Ar) identifiziert. Cc und Va wurden bei allen pH-Werten gebildet, während Ar nur bei $\text{pH} \geq 10.00$ auftrat. Bei hohen pH-Werten ist die ACAR deutlich höher als bei niedrigen pH Werten, wodurch die Nukleation von CaCO_3 früher beginnt. Interessanterweise, war bei einer gesamten experimentellen Zeit von 20 Stunden die Menge an ausgefällten CaCO_3 ähnlich für alle Experimente. Dies lässt sich durch die Abnahme der R_{CaCO_3} mit steigenden pH-Wert erklären, welche durch die generellen Abnahme der Konzentration des CaHCO_3^0 Komplexes an der CaCO_3 -Oberfläche bewirkt wird. Die Quantifizierung von CaCO_3 wird somit durch die Kombination der CO_3^{2-} Akkumulations- und CaCO_3 Abscheidungskinetik bestimmt. Weiteres wurde in der vorliegenden Studie die Kopräzipitation von B und Sr mit CaCO_3 und die O-Isotopenzusammensetzung von CaCO_3 untersucht. Während die Ausfällung von B mit CaCO_3 und die Fraktionierung der $^{18}\text{O}^{16}\text{O}$ -

Isotope stark vom pH Wert der Lösung abhängen, wird der Einbau von Sr im gesamten CaCO_3 durch den Anteil von Ar bestimmt.

TABLE OF CONTENTS

AKNOWLEDGEMENTS

ABSTRACT

KURZFASSUNG

1. INTRODUCTION.....	1
2. THEORETICAL BACKGROUND.....	3
2.1 CaCO ₃ modifications.....	3
2.2 Dissolved inorganic carbon species.....	3
2.3 Solubility of CaCO ₃ polymorphs.....	4
2.4 Gas-solution exchange and CaCO ₃ precipitation mechanisms.....	5
2.5 Sr incorporation into CaCO ₃	6
2.6 Stable oxygen isotopes in CaCO ₃ precipitates	7
2.7 Boron incorporation into CaCO ₃	8
3. METHODOLOGY.....	10
3.1 Laboratory experiments	10
3.1.1 Experimental set up.....	10
3.1.2 Experimental background	11
3.1.3 Estimation of titration curve parameters	12
3.1.3.1 CO ₂ uptake rate and aqueous carbonate accumulation rate.....	13
3.1.3.2 Precipitation rate of CaCO ₃	14
3.2 Analytical methods	14
3.2.1 Solution chemistry	14
3.2.2 Solid phase characterization.....	15
3.2.3 Isotopic composition	15
4. RESULTS.....	16
4.1 Solid phase characterization	16
4.2 Accumulation and Precipitation kinetics	22
4.2.1 First detection of CaCO ₃ formation and crystal growth time.....	22
4.2.2 CO ₂ uptake and aqueous carbonate accumulation rate.....	28
4.2.3 Precipitation rate of CaCO ₃	28

4.2.4 Recalculation of UT_{CO_2}	29
4.2.5 Ion activity product for $CaCO_3$ and saturation index with respect to calcite	31
4.3 Coprecipitation of Sr and B with $CaCO_3$	32
4.3.1 Sr coprecipitation	32
4.3.2 B coprecipitation	33
4.4 Stable oxygen isotopes	34
5. DISCUSSION	35
5.1 Uptake rate of CO_2	35
5.2 Aqueous carbonate accumulation rate	38
5.3 $CaCO_3$ nucleation and growth	40
5.4 Precipitation rates of $CaCO_3$	42
5.5 $CaCO_3$ modifications	45
5.6 Coprecipitation of strontium with $CaCO_3$	46
5.7 Coprecipitation of boron with $CaCO_3$	48
5.8 Oxygen isotopes	50
6. SUMMARY AND CONCLUSION	51
7. REFERENCES	54
8. APPENDIX	58

1. INTRODUCTION

Calcium carbonates (CaCO_3) are of great concern in natural and man-made environments. Naturally formed carbonate minerals comprise about 10-15 wt. % of the Earth crust's sediments, mainly originated from biological activity (e.g. Dietzel, 2011). Organisms like corals, mussels and calcareous plankton induce precipitation of CaCO_3 for their skeletons and thus accomplish an important role in elemental cycles of the Earth (Orr et al., 2009). However, naturally formed carbonates comprise also a huge variety of inorganic precipitates in marine and terrestrial systems such as evaporites, speleothems, travertines, and alkaline lake deposits (Morse and Mackenzie, 1990).

In principle the formation of CaCO_3 can be induced by CO_2 degassing or absorption depending on the respective pH and DIC content (e.g. Rinder et al., 2013). CaCO_3 precipitation caused by the uptake of CO_2 can be followed through travertine formation from natural alkaline solutions (e.g. Clark et al., 1992). Analogous CO_2 uptake in alkaline solutions occurs in anthropogenic environments. For instance in drainage systems highly alkaline and Ca^{2+} -rich solutions, which are formed through the dissolution of portlandite ($\text{Ca}(\text{OH})_2$) from concrete, absorption of atmospheric CO_2 , and subsequently precipitation of CaCO_3 (e.g. Dietzel et al., 1992). Moreover, industrial applications are based on the uptake of CO_2 in slurries of slaked lime, where tailored CaCO_3 precipitates are used e.g. as pigments and fillers (Park et al., 2004). The induced precipitation of CaCO_3 in calcium-enriched, alkaline solutions is also valid for CO_2 sequestration issues, where alkaline reacting minerals or rocks are proposed for CO_2 capture (e.g. Back et al., 2011; Montes-Hernandez et al., 2012).

Once the ion activity product (IAP) threshold for nucleation and precipitation of CaCO_3 is reached distinct CaCO_3 polymorph formation occur. The CaCO_3 formation behavior depends on the present physico-chemical conditions like temperature, pH, ionic strength, inorganic and organic additives, accumulation rate of aqueous carbonate, presence of seeds etc. (Morse et al., 1997; Niedermayr et al., 2013).

For the reconstruction of environmental conditions and monitoring issues during the precipitation process of CaCO_3 trace elements (e.g. Sr^{2+} and Mg^{2+}) and stable isotopes (e.g. O-, C- and B-isotopes) are commonly used. For instance Sr^{2+} , which is incorporated into CaCO_3 , infers temperatures and precipitation rates during distinct CaCO_3 formation (e.g. Lorens, 1981; Tang et al., 2008). The distribution of $^{18}\text{O}/^{16}\text{O}$ in biogenic carbonates or speleothems can yield in paleotemperatures assuming equilibrium isotope fractionation (Erez et al., 1983 and Spötl et al., 2003). In contrast, in strong alkaline surroundings $^{18}\text{O}/^{16}\text{O}$ and $^{13}\text{C}/^{12}\text{C}$ signatures

of CaCO₃ precipitates can be used to distinguish precipitation reaction mechanisms and carbonate sources, which is based on the hydroxylation of CO₂ and disequilibrium isotope fractionation effects (Clark et al., 1992; Dietzel, 2000). The incorporation and isotopic composition of boron in CaCO₃ is of current interest to reconstruct the pH during its formation, which is applied e.g. to marine environments to discover the evolution of the Earth's climate (Allen et al., 2012; Ruiz-Agudo et al., 2012).

Although, CO₂ absorption in alkaline, calcium-bearing solutions is well known in natural and man-made environments, significant gaps of knowledge exist for (i) the combined reaction kinetics (CO₂ uptake and CaCO₃ precipitation) in alkaline solutions as well as (ii) distinct CaCO₃ polymorph formation. The aim of the present study is to evaluate potential impacts of the pH on the aqueous carbonate accumulation rate caused by CO₂ uptake and overall CaCO₃ precipitation kinetics. Therefore, CaCO₃ precipitation experiments were carried out from pH 8.30 to 11.50 by using a CO₂ diffusion technique. At distinct pH the occurrence and quantity of CaCO₃ polymorphs are studied. A further focus is given on the incorporation of Sr²⁺ and B into CaCO₃ and on the fractionation of stable oxygen isotopic during the individual experiments.

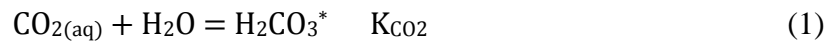
2. THEORETICAL BACKGROUND

2.1 *CaCO₃ modifications*

The minerals calcite, aragonite and vaterite are the anhydrous polymorphs of calcium carbonates (CaCO₃). Calcite, the thermodynamically stable CaCO₃ polymorph at standard conditions, has a trigonal symmetry and is an essential mineral in sedimentary rocks and sediments (Mackenzie and Morse, 1992; Morse and Arvidson, 2002). The orthorhombic aragonite can be formed e.g. in marine environments by inorganic or biological processes and thus is common in recent marine sediments (Berndt and Seyfried, 1999; Gaetani and Cohen, 2006). Aragonite is thermodynamically metastable under standard conditions and tends to alter to calcite after deposition (Hover et al., 2001). Vaterite, which has a hexagonal symmetry, is less stable than calcite and aragonite and is generally not preserved in sediments (Gussone et al., 2011). The metastable mineral vaterite is rarely occurring in nature, but found e.g. as biogenic material in cultured pearls of freshwater bivalves (Ma et al., 2013) and in fish otoliths (Gauldie et al., 1997). The formation of calcite, aragonite and vaterite strongly depends on the temperature, reaction kinetics and additives such as organics or Mg²⁺ (Niedermayr et al., 2012).

2.2 *Dissolved inorganic carbon species*

As gaseous CO₂ dissolves in water the following DIC (dissolved inorganic carbon) species are formed: aqueous carbon dioxide (CO_{2(aq)}), carbonic acid (H₂CO₃), bicarbonate ion (HCO₃⁻) and carbonate ion (CO₃²⁻) (Appelo et al., 2010). CO_{2(aq)} is about a factor of 1000 more abundant than H₂CO₃. Thus for simplification a combined H₂CO₃^{*} concentration is defined ([H₂CO₃^{*}] = [CO_{2(aq)}] + [H₂CO₃], where []: molar concentration). The distribution of DIC species depend mainly on the pH of the solution. The following equations describe the fundamental reactions between aqueous CO₂ and H₂O



(Stumm and Morgan, 1996).

The equilibrium constants (K) are determined by the activity of reactants and products according to the expressions

$$K_{\text{CO}_2} = \frac{(\text{H}_2\text{CO}_3^*)}{P_{\text{CO}_2} \cdot (\text{H}_2\text{O})} = 10^{-1.47} \quad (4)$$

$$K_1 = \frac{(\text{H}^+) \cdot (\text{HCO}_3^-)}{(\text{H}_2\text{CO}_3)} = 10^{-6.35} \quad (5)$$

$$K_2 = \frac{(\text{H}^+) \cdot (\text{CO}_3^{2-})}{(\text{HCO}_3^-)} = 10^{-10.33} \quad (6)$$

where K values are given for 25°C and 1 atm from Usdowski (1982). The equations show that at pH < 6.3 H₂CO₃^{*} is predominant, whereas at 6.3 < pH < 10.3 HCO₃⁻ dominates the DIC. At pH > 10.3 CO₃²⁻ is the dominant DIC species. In summary, the [CO₃²⁻]/[DIC] ratio of a solution increases with increasing pH

2.3 Solubility of CaCO₃ polymorphs

The solubility of CaCO₃ polymorphs is expressed by the individual solubility product, K_s = (Ca²⁺) · (CO₃²⁻), which represents the activity product of the respective mineral under thermodynamic equilibrium conditions at a given temperature (Dietzel, 2011). At a temperature of 25°C the solubility product of calcite, 10^{-8.48}, is less than that of aragonite and vaterite, 10^{-8.34} and 10^{-7.91}, respectively (data from Plummer and Busenberg, 1982). Hence, calcite is the thermodynamically stable CaCO₃ polymorph at 25°C. The solubility of CaCO₃ minerals decrease with increasing temperature. Furthermore, the solubility of CaCO₃ depends on pressure conditions, where an elevated pressure causes an increase of solubility. Another influencing factor is the ionic strength of the solution. Elevated ionic strength is associated with lower ion activity coefficients, which stimulates the dissolution of CaCO₃. The solubility of CaCO₃ is also influenced by the formation of aquo complexes, which consist e.g. of Ca²⁺ ions and ligands such as carbonates or phosphates. The formation of aquo complexes can significantly reduce the activity of dissolved Ca²⁺ (and/or CO₃²⁻), thus the solubility of CaCO₃ increases.

The saturation index (SI_{calcite}) indicates whether for instance calcite may dissolve or precipitate by comparing the measured ion activity product, $IAP = (Ca^{2+}) \cdot (CO_3^{2-})$, of the solution with the given solubility product of calcite (K_{calcite}) according to the equation

$$SI_{\text{calcite}} = \log \frac{(Ca^{2+}) \cdot (CO_3^{2-})}{K_{\text{calcite}}} = \log \frac{IAP}{K_{\text{calcite}}} \quad (7)$$

As the solution is supersaturated with respect to calcite ($SI > 0$), precipitation of $CaCO_3$ may occur. Conversely, calcite has to be dissolved at $SI < 0$ until thermodynamic equilibrium between solid and solution is reached ($SI = 0$).

2.4 Gas-solution exchange and $CaCO_3$ precipitation mechanisms

Water, which gets into contact with the Earth's atmosphere, may degas or absorb CO_2 depending on the CO_2 partial pressure (P_{CO_2} in atm). If the internal P_{CO_2} of the solution (estimated P_{CO_2} at thermodynamic equilibrium with the solution) is higher than that of the Earth's atmosphere ($P_{CO_2} = 10^{-3.5}$ atm), CO_2 degasses until an internal $P_{CO_2} = 10^{-3.5}$ atm is reached. Conversely, CO_2 is absorbed into the solution, if the internal P_{CO_2} of the solution is less than that of the Earth's atmosphere.

Various processes, which are based on the exchange of CO_2 between a gas phase and an aqueous solution, can cause precipitation of carbonate minerals. $CaCO_3$ formation, caused by CO_2 degassing, occurs in terrestrial systems for instance in spring water or in drip water of caves. DIC rich water, which comes into contact with the Earth's atmosphere, degasses CO_2 due to the lower atmospheric versus the internal P_{CO_2} . This leads to an increase of the pH and $[CO_3^{2-}]/[HCO_3^-]$ ratio in the solution. As soon as an IAP threshold is reached precipitation of $CaCO_3$ starts. The formation of $CaCO_3$ by the uptake of CO_2 plays an important role in alkaline solutions. For instance in man-made surroundings groundwater may dissolve portlandite ($Ca(OH)_2$) from concrete, which results in elevated concentrations of Ca^{2+} and OH^- ions in the solution. When the resulting alkaline water comes into contact with the Earth's atmosphere, CO_2 is absorbed and is rapidly "transformed" to CO_3^{2-} due to the high pH of the solution, which finally may yield in carbonate scaling.

2.5 Sr incorporation into CaCO₃

Ca²⁺ ions can be substituted in the crystal lattice of calcium carbonate minerals by other divalent ions like Mg²⁺ and Sr²⁺. The isomorphic substitution depends on the crystal symmetry and the ionic size of the divalent ion. Cations with a smaller ionic radius than that of Ca²⁺ (e.g. Fe²⁺, Mg²⁺, Mn²⁺, Cd²⁺ and Zn²⁺) are preferentially incorporated in the structure of calcite (6-coordination with respect to oxygen), while larger ions like Ba²⁺, Sr²⁺, Pb²⁺ are favored in the aragonite structure, which has a 9-coordination (Reeder, 1990). Thus, Mg²⁺ prefers the trigonal calcite structure, whereas Sr²⁺ is easier incorporated in the orthorhombic structure of aragonite. In principle, such an incorporation of trace elements can be used for the reconstruction of environmental conditions during CaCO₃ formation. For instance Sr²⁺/Ca²⁺ ratios of marine CaCO₃ shells or speleothems provide information about paleotemperatures (De Villiers, 1994; Huang et al., 2001). The incorporation of e.g. Sr²⁺ into the CaCO₃ lattice is defined by the distribution coefficient according to the equation

$$D_{\text{Sr}} = \frac{\left(\frac{[\text{Sr}]}{[\text{Ca}]}\right)_{\text{s}}}{\left(\frac{[\text{Sr}]}{[\text{Ca}]}\right)_{\text{aq}}} \quad (8)$$

which expresses by the molar ratio of Sr²⁺ to Ca²⁺ in the solid (s) versus the molar ratio in the aqueous solution, ([Sr]/[Ca])_{aq} (e.g. Tang et al., 2008 for calcite). This equation is only valid for a homogenous Sr²⁺ distribution during CaCO₃ precipitation in open systems, when the solution composition does not significantly change during CaCO₃ formation. At closed system conditions with respect to the solution volume a heterogeneous distribution of Sr²⁺ occurs during the precipitation and the evolution of the initial aqueous molar Ca²⁺ concentration ([Ca]₀)_{aq} over precipitation time has to be considered according to the equation

$$\left(\frac{[\text{Sr}]}{[\text{Ca}]}\right)_{\text{s}} = \left(\frac{[\text{Sr}]}{[\text{Ca}]}\right)_{\text{aq},0} \cdot \frac{1 - \left(\frac{[\text{Ca}]}{[\text{Ca}]_0}\right)_{\text{aq}}^{D_{\text{Sr}}}}{1 - \left(\frac{[\text{Ca}]}{[\text{Ca}]_0}\right)_{\text{aq}}} \quad (9)$$

(Tang et al., 2008). Equation 9 yields in the expression

$$D_{\text{Sr}} = \frac{\log \left\{ 1 - \frac{\left(\frac{[\text{Sr}]}{[\text{Ca}]}\right)_s}{\left(\frac{[\text{Sr}]}{[\text{Ca}]}\right)_{\text{aq},0}} \cdot \left[1 - \left(\frac{[\text{Ca}]}{[\text{Ca}]_0}\right)_{\text{aq}} \right] \right\}}{\log \left[\left(\frac{[\text{Ca}]}{[\text{Ca}]_0}\right)_{\text{aq}} \right]} \quad (10)$$

where $([\text{Sr}]/[\text{Ca}]_s)$ is the ratio of the molar Sr^{2+} and Ca^{2+} concentration of the precipitated solid at the end of the experiment, $([\text{Sr}]/[\text{Ca}]_{\text{aq},0})$ denotes the initial molar $\text{Sr}^{2+}/\text{Ca}^{2+}$ ratio of the outer solution and $([\text{Ca}]/[\text{Ca}]_0)_{\text{aq}}$ is the molar ratio of the Ca^{2+} concentration of the outer solution after a certain crystallization time to the initial $[\text{Ca}]_0$.

For each CaCO_3 modification an individual D_{Sr} value is valid at thermodynamic equilibrium (Böttcher and Dietzel, 2010). The D_{Sr} value depends on the temperature and can be used e.g. as an indicator for precipitation rates at a given temperature caused by non-equilibrium effects (e.g. Lorens, 1981; Tang et al., 2008 for calcite).

2.6 Stable oxygen isotopes in CaCO_3 precipitates

Oxygen isotopes can be used as proxies with regard to environmental formation conditions of CaCO_3 minerals in marine or terrestrial systems. The fractionation behavior of $^{18}\text{O}/^{16}\text{O}$ at isotopic equilibrium between CaCO_3 (considering also DIC) and H_2O can indicate the water temperature at which CaCO_3 was formed and is therefore widely used in paleoclimate research (e.g. Ghosh et al., 2006).

The $^{18}\text{O}/^{16}\text{O}$ ratio of a CaCO_3 sample is compared to a standard according to the equation

$$\delta^{18}\text{O}_{\text{sample}} = \frac{\left(\frac{^{18}\text{O}}{^{16}\text{O}}\right)_{\text{sample}} - \left(\frac{^{18}\text{O}}{^{16}\text{O}}\right)_{\text{standard}}}{\left(\frac{^{18}\text{O}}{^{16}\text{O}}\right)_{\text{standard}}} \cdot 1000 \quad (11)$$

$\delta^{18}\text{O}$ values are given in ‰, where the VSMOW (Vienna Standard Mean Ocean Water) or VPDB (Vienna Pee Dee Belemnite) is used (Hoefs, 2009).

The so-called isotope fractionation factor ($\alpha_{\text{A-B}}$) is based on the respective isotope ratio measurements of two phases A and B

$$\alpha_{A-B} = \frac{R_A}{R_B} \quad (12)$$

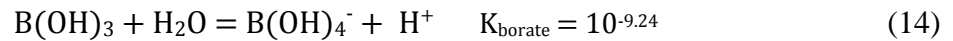
where for the two phases A and B, their δ -values and α_{A-B} are related by

$$1000 \ln \alpha_{A-B} \approx \Delta_{A-B} = \delta_A - \delta_B \quad (13)$$

The fractionation of stable oxygen isotopes at isotopic equilibrium between CaCO_3 and H_2O varies with temperature (Urey, 1947; O'Neil, 1977), but is also affected by pH and reaction kinetics, which is valid especially in alkaline environments (Dietzel et al., 2009). Thus, both equilibrium and kinetic isotope effects have to be considered by using stable isotopes of oxygen for the evaluation of paleotemperatures and -environments (Hoefs, 2009; Dietzel et al., 1992).

2.7 Boron incorporation into CaCO_3

Aqueous boron is present as trigonal boric acid (B(OH)_3) and tetrahedral borate (B(OH)_4^- : tetrahydroxyborate). The distribution of these two boron species depends strongly on pH. The reversible conversion of B(OH)_3 to B(OH)_4^- is given by the following hydrolysis reaction



According to this reaction the concentration of B(OH)_4^- becomes dominant over B(OH)_3 above pH 9.24. The activity of boron species versus pH for our experimental conditions is given in Fig. 1. The activity of B(OH)_3 decreases at elevated pH, whereas the activity of individual boron species, such as B(OH)_4^- and CaB(OH)_4^+ increases. The similarity between the boron isotopic composition of marine carbonates and of the B(OH)_4^- in sea water suggests that borate is the aqueous species, which is preferentially incorporated into marine carbonates (Hemming and Hanson, 1992). Based on this assumption the $[\text{B}]/[\text{Ca}]$ ratio of the precipitated CaCO_3 should increase with increasing pH. This aspect and respective boron isotope fractionation effects can be used as a proxy for the pH during CaCO_3 formation (Ruiz-Agudo et al., 2012; Hoefs, 2009).

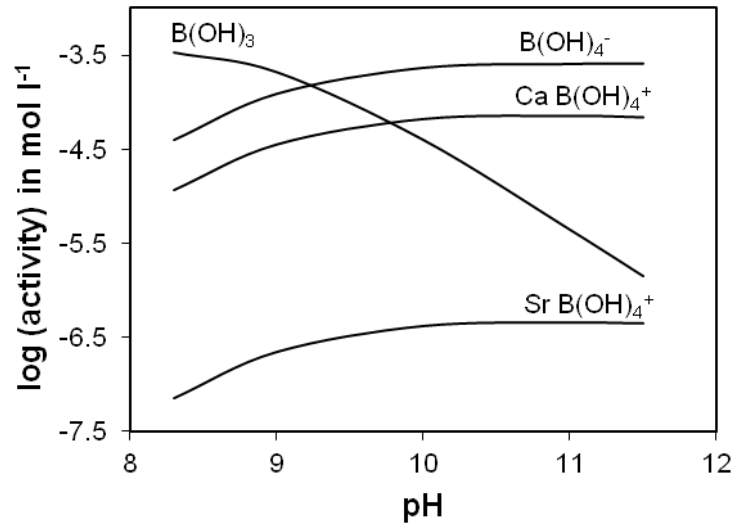


Fig. 1. Activity of boron species as a function of pH at $[B] = 0.4 \text{ mmol L}^{-1}$ and 25°C (modeled using PHREEQ C).

3. METHODOLOGY

3.1 Laboratory experiments

Calcium carbonate was precipitated by using a CO₂-diffusion technique (Tang et al., 2008) as displayed in Fig. 2. This technique is based on the diffusion of CO₂ through a membrane from an inner into an outer Ca²⁺ bearing solution (Fig. A1a). The CO₃²⁻ content in the outer solution increases until an IAP threshold for CaCO₃ precipitation is reached (Fig. A1b). In the present study two analogous sets of experiments were carried out in a temperature-controlled water bath.

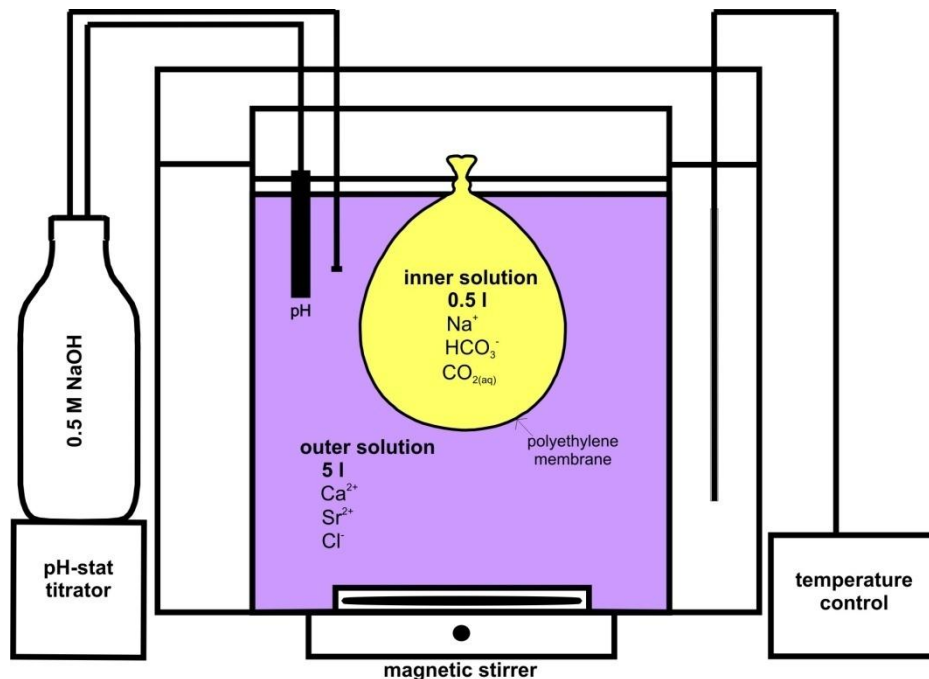


Fig. 2. Experimental setup of the CO₂-diffusion technique for the precipitation of CaCO₃.

3.1.1 Experimental set up

A polyethylene (PE) bag with a membrane thickness of 0.2 mm and a surface area of $6.2 \cdot 10^4$ mm² separates the inner from the outer solution (Fig. 2). The inner solution (0.5 L) contains 35g NaHCO₃, which leads to an internal CO₂ partial pressure (P_{CO_2}) of $10^{-0.20}$ atm. The outer solution (5 L), which was prepared in an acrylic glass vessel, contains 10 mM CaCl₂, 0.1 mM SrCl₂ and 0.4 mM NaBO₂, whereas the latter has been omitted in the first set of experiments. The selected concentrations of Ca²⁺, Sr²⁺ and B are similar to modern sea water. The chemicals (pro analyses grade CaCl₂·2H₂O, SrCl₂·6H₂O, NaBO₂·4H₂O and NaHCO₃) were dissolved in Milli-Q water (Millipore Integral 3: 18.2 MΩcm⁻¹) for preparing the inner and outer solution. The pH value of the outer solution was kept constant at 8.30,

9.00, 10.00, 11.00 and 11.50 by adding 0.5 M NaOH solution using an automated pH_{stat} titrator (Schott TitroLine alpha plus titrator at ± 0.03 pH_{stat} for 10 μl titration steps). During the experimental run the pH of the outer solution was measured with a Schott BlueLine 28 combination electrode calibrated with standard pH 4.01, 7.00 and 10.00 buffer solutions (25°C).

The reaction vessel, which contains the outer solution, was placed into a thermostatic water bath (Huber ministat 230 CCC2) to keep the temperature of the solutions at $25 \pm 0.5^\circ\text{C}$. The solution was continuously stirred at 150 rpm using a floating stirring bar (Variomag Maxi Direct) to reach homogenization and to avoid grinding of precipitates. The bag, which contains the inner solution, was placed into the glass vessel as soon as the pH of the outer solution was adjusted. During the experimental run the exchange between the outer solution and the laboratory atmosphere was prevented by an airtight cap. The chemical evolution of the outer solution was monitored by taking samples of 10 ml at certain time intervals during the experiment. In addition, samples of 40 ml were taken at the beginning and at the end of each experimental run for oxygen isotope analyses of the H_2O . All taken samples were filtered through a 0.2 μm cellulose acetate membrane. After reaching a total experimental time of ≈ 20 h, the entire outer solution was filtered through a 0.2 μm cellulose acetate filter using a vacuum filtration unit to receive the precipitates. The separated solids were dried at 40°C and prepared for solid phase characterization.

The concentrations of aqueous species, the ion activity product and the saturation index with respect to CaCO_3 polymorphs in the outer solution at a certain experimental time were modeled using PHREEQC 2.0 with minteq.v4 database.

3.1.2 Experimental background

During the experiment CO_2 diffuses from the inner into the outer solution due to the CO_2 partial pressure gradient between both solutions. When CO_2 reacts with H_2O in the outer solution, H^+ is produced during the dissociation steps of carbonic acid into HCO_3^- and CO_3^{2-} (equations 2 and 3). Hence, NaOH is added to keep the pH constant (pH_{stat}). Therefore, the amount of added volume of 0.5 M NaOH solution vs. time reflects the CO_2 uptake into the outer solution. As soon as an IAP threshold is reached through the accumulation of CO_3^{2-} , CaCO_3 is formed according to the equation



CO_3^{2-} ions, which are removed through CaCO_3 formation, will be replaced by newly dissociated CO_3^{2-} ions from H_2CO_3 and HCO_3^- . The additionally produced H^+ (besides CO_2 uptake) requires additional volumes of NaOH solution to maintain pH_{stat} conditions. Therefore, the evolution of the NaOH addition vs. experimental time of individual experiments reflects parameters as the CO_2 uptake rate, the time of first crystallization and the precipitation rate.

3.1.3 Estimation of titration curve parameters

A typical evolution of the NaOH solution addition during an experiment is shown by the titration curve in Fig. 3 (pH 8.30). Four periods can be distinguished during the consumption of OH^- . The first period of the experiment (I) is characterized by the continuous diffusion of CO_2 through the PE membrane from the inner into the outer solution. As mentioned before, the NaOH addition balances the CO_2 uptake in the outer solution at pH_{stat} conditions. Therefore, the amount of added NaOH solution over time reflects the CO_2 uptake rate, which can be calculated in this period. The beginning of the second period (II) is defined by the time of first net nucleation of CaCO_3 (t_{fc}) in the outer solution, which was determined by the minimum of the first derivation of the titration curve (see Fig. A2). In period II, elevated amounts of NaOH solutions are added to keep the pH constant during ongoing CaCO_3 nucleation and crystallization besides CO_2 uptake. The intersection point of the regression lines A and B indicates - from now on - the dominance of CaCO_3 crystal growth vs. CO_2 uptake for the titration curve (period III). Larger quantities of OH^- are consumed in this period. Finally (period IV) the NaOH addition rate decreases in comparison with period III. t_g indicates the growth time of calcium carbonate crystals, which begins at intersection point until the end of the experiment (end of period IV).

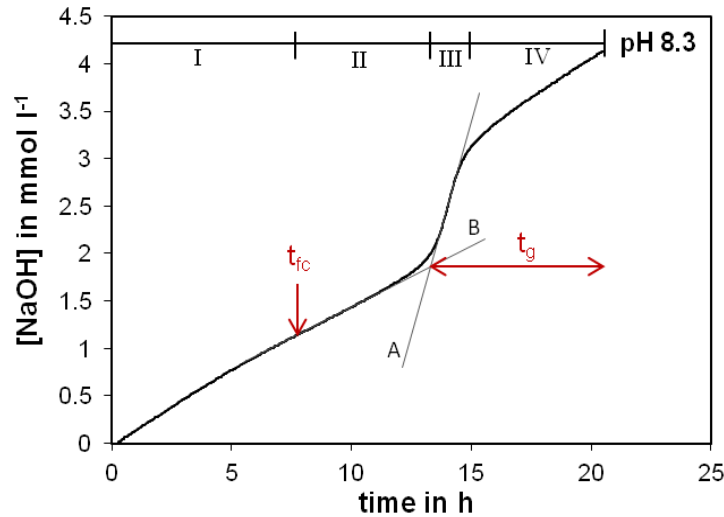


Fig. 3. NaOH addition in the outer solution during the experimental time run at pH 8.30 (#1). t_{fc} and t_g denote the time for the detection of the first net CaCO_3 nucleation and the CaCO_3 crystal growth time during periods III and IV, respectively.

3.1.3.1 CO_2 uptake rate and aqueous carbonate accumulation rate

The average CO_2 uptake rate ($UT_{\text{CO}_2\text{av}}$ in $\mu\text{mol h}^{-1} \text{l}^{-1}$) in the outer solution, was calculated by the total amount of added NaOH solution (in $\mu\text{mol l}^{-1}$) until t_{fc} is reached according to equation

$$UT_{\text{CO}_2\text{av}} = f_1(T, \text{pH}) \cdot \frac{\text{NaOH}_{fc}}{t_{fc}} \quad (16)$$

(see Niedermayr et al., 2013). The conversion factor f_1 considers the total amount of added OH^- with regard to the dissociation of H_2CO_3 to HCO_3^- and CO_3^{2-} and to the formation of CO_3^{2-} containing aquo complexes like e.g. CaCO_3^0 and SrCO_3^0 . At pH 8.30 the CO_2 is mainly converted to HCO_3^- and 1 mol OH^- per 1 mol HCO_3^- is approximately required to maintain pH_{stat} conditions. In contrast, at pH 11.50 CO_3^{2-} dominates the DIC and the dissociation of CO_2 into CO_3^{2-} requires about 2 mol of OH^- for 1 mol of CO_3^{2-} . Therefore, the factor f_1 ranges from about 1 to 0.5 from pH 8.30 to 11.50.

The aqueous carbonate accumulation rate (ACAR in $\mu\text{mol h}^{-1} \text{l}^{-1}$) was calculated by multiplying the $UT_{\text{CO}_2\text{av}}$ with the molar ratio of the carbonate species to the DIC of the solution according to the equation

$$\text{ACAR} = \frac{[\text{CO}_3^{2-}][\text{CaCO}_3^0][\text{SrCO}_3^0]}{[\text{DIC}]} \cdot UT_{\text{CO}_2\text{av}} \quad (17)$$

(Niedermayr, 2013). The molar concentrations of the aqueous species were calculated using PHREEQC by considering the temperature, the pH of the outer solution and the measured chemistry of the outer solution.

3.1.3.2 Precipitation rate of CaCO_3

The formation of CaCO_3 can be followed by the decrease of the Ca^{2+} concentration in the outer solution. Thus, the overall precipitation rate of CaCO_3 (R_{CaCO_3} in $\mu\text{mol h}^{-1} \text{ l}^{-1}$) was calculated by consumed measured $[\text{Ca}]$ during periods III and IV according to the equation

$$R_{\text{CaCO}_3} = \frac{[\Delta\text{Ca}]}{\Delta t} \quad (18)$$

The consumed Ca^{2+} concentration at a certain time (t_i) during the experiment can be also derived from the titration curve by the equation

$$[\text{Ca}]_{t_i} = f_2(T, \text{pH}) \cdot ([\text{NaOH}]_{t_i} - [\text{NaOH}_{\text{CO}_2}]_{t_i}) \quad (19)$$

where $[\text{NaOH}]_{t_i}$ is the total added molar concentration of NaOH solution until t_i . $[\text{NaOH}_{\text{CO}_2}]_{t_i}$ is the proportion of $[\text{NaOH}]_{t_i}$, which was added into the outer solution to balance the CO_2 uptake ($[\text{NaOH}_{\text{CO}_2}]_{t_i} = ([\text{NaOH}]_{f_c}/t_{f_c}) \cdot t_i$). The conversion factor f_2 is expressed by the ratio of $[\text{DIC}]$ to $[\text{HCO}_3^-]$ and ranges from 1.08 to 109.5 between pH 8.30 and 11.50, respectively. At pH 8.30 HCO_3^- dominates the DIC species in the outer solution and the formation of CaCO_3 causes additional produced H^+ through the conversion of HCO_3^- to CO_3^{2-} . The ratio of $[\text{CO}_3^{2-}]$ to $[\text{HCO}_3^-]$ increases with increasing pH and at pH 11.50 the DIC species are almost completely present as CO_3^{2-} . Therefore, less HCO_3^- must be converted to CO_3^{2-} and less NaOH solution is added into the outer solution during the precipitation of CaCO_3 at elevated pH.

3.2 Analytical methods

3.2.1 Solution chemistry

The filtered and diluted solutions were analyzed by ion chromatography for ion content (Dionex IC S 3000). The boron content in the B-bearing solutions of the second set of experiments was measured with ICP-Mass Spectrometry (Agilent 7500). The precision of the IC and ICP-MS measurements is about ± 3 and 5 %, respectively

3.2.2 Solid phase characterization

The dried precipitates were analyzed by XRD (X-Ray-Diffraction, PANalytic X-ray Powder Diffractometer X'Pert Pro) for CaCO₃ polymorphism. The XRD analyses were carried out using Cobalt K_α-radiation (40mA, 40kV) at a 2θ range from 4° to 85°. The CaCO₃ polymorphs were quantified by using distinct peak areas (A_i) from XRD pattern according to the equations

$$X_{Cc} = \frac{1}{1 + 6.4 \frac{A_{Ar221}}{A_{Cc104}} + 5.7 \frac{A_{Vat110}}{A_{Cc104}}} \quad (20)$$

$$X_{Ar} = 6.4 \frac{A_{Ar221}}{A_{Cc104}} X_{Cc} \quad (21)$$

$$X_{Vat} = 1 - X_{Cc} - X_{Ar} \quad (22)$$

(adapted from Kontoyannis and Vagenas, 2000). The areas of the reflection peaks at d₁₀₄ (3.035 Å) for calcite, d₂₂₁ (1.973 Å) for aragonite and d₁₁₀ (3.573 Å) for vaterite were used for quantification. The values 6.4 and 5.7 are proportionality constants obtained by in-house calibration (Niedermayr, 2013). The bulk solid phases were also characterized by ATR-FTIR (Attenuated Total Reflectance - FT-Infrared Spectroscopy, Perkin Elmer Spektrum 100) in the range from 450 to 4000 cm⁻¹. Selected crystals of the precipitates were analysed by micro-Raman spectroscopy (Jovin Yvon Labram HR 800) using a green laser (532 nm) with a spot diameter size of about 2 μm. The Raman spectra were obtained in a range between 100 and 1200 cm⁻¹. Imaging of individual crystals was realized by Scanning Electron Microscopy (SEM, ZEISS DSM 982 Gemini at 5 kV with gold coated samples). Small amounts of the precipitates were dissolved in 2% bidistilled HNO₃ and analyzed by IC and ICP-MS for their chemical composition.

3.2.3 Isotopic composition

The ¹⁸O/¹⁶O isotopic composition of the H₂O from the outer solution was measured using CF-IRMS (Continuous Flow Isotope Ratio Mass Spectroscopy, Finnigan Delta^{plus}) at the beginning and the end of each experiment. The received precipitates were analyzed with mass spectroscopy for oxygen isotopes using the common phosphoric acid method (Dietzel et al., 2009). All analyses are given relative to VPDB (Vienna Pee Dee Belemnite Standard) in %.

4. RESULTS

4.1 Solid phase characterization

The XRD patterns for the boron-free (set 1) and boron-containing experiments (set 2) are given in Figs. 4a and 4b, respectively. Calcite, aragonite and vaterite were identified by their characteristic peaks at $d_{104} = 3.04 \text{ \AA}$, $d_{111} = 3.39 \text{ \AA}$ and $d_{112} = 3.57 \text{ \AA}$, respectively. The calculated fractions of calcite (X_{Cc}), aragonite (X_{Ar}) and vaterite (X_{Va}) in wt. % are obtained from XRD pattern according to the equations 20-22 (Tab. 1). Calcite and vaterite were precipitated in all experiments, whereas aragonite was only present at $\text{pH} \geq 10.00$. The maximal amount of aragonite was precipitated at $\text{pH} 11.00$ (experiment #4; 87 wt. %). Vaterite dominates between $\text{pH} 8.30$ and 10.00 (63 ± 13 wt. %) and is formed as minor component at $\text{pH} \geq 11.00$ (6 ± 5 wt. %). Calcite is present at all pH values with > 10 wt. % and shows a maximum at $\text{pH} 11.50$ (67 ± 14 wt. %). The absence and present of traces of boron (4 mg/L) show no all-over trend in the occurrence of CaCO_3 polymorph.

The results from XRD analyses are confirmed by FTIR, where calcite, aragonite and vaterite were identified by the in-plane bending vibration (ν_4) of the carbonate group (Fig. 5). Aragonite displays adsorption peaks at 700 and 712 cm^{-1} , whereas calcite and vaterite are characterized by a single adsorption peak at wave numbers 712 and 745 , respectively (Niedermayr et al., 2013).

Besides bulk analyses single crystals were analyzed by Raman Spectroscopy. An optical microscopy image of calcite, aragonite and vaterite crystals from experiment #5 ($\text{pH} 11.50$) is shown in Fig. 6a. The respective Raman spectra for the marked areas in Fig. 6a are exemplarily given in Figs. 6b to 6d for calcite, aragonite and vaterite, respectively. Calcite can be easily distinguished from aragonite and vaterite by less adsorption at 156 , 283 and 712 cm^{-1} , whereas vaterite is characterized by a sequence of adsorption peaks between 100 and 350 cm^{-1} and a strong peak at 751 cm^{-1} . The characteristic adsorption peaks for aragonite are 155 , 208 and 706 cm^{-1} .

SEM images of calcite, aragonite and vaterite are shown in Fig. 7. Calcite crystals exhibit rhombohedral shape with 10 - $20 \text{ }\mu\text{m}$ in size. Maximum crystal sizes of about $40 \text{ }\mu\text{m}$ are reached at $\text{pH} 11.50$. Aragonite has a dipyramidal, spicular form with needle sizes between 5 and $10 \text{ }\mu\text{m}$. Vaterite is present as roughly hexagonal plates, which are composed of aggregates of single crystals. The vaterite plates have typical diameters between 3 and $10 \text{ }\mu\text{m}$, but individual plates reach a maximal size of up to $15 \text{ }\mu\text{m}$.

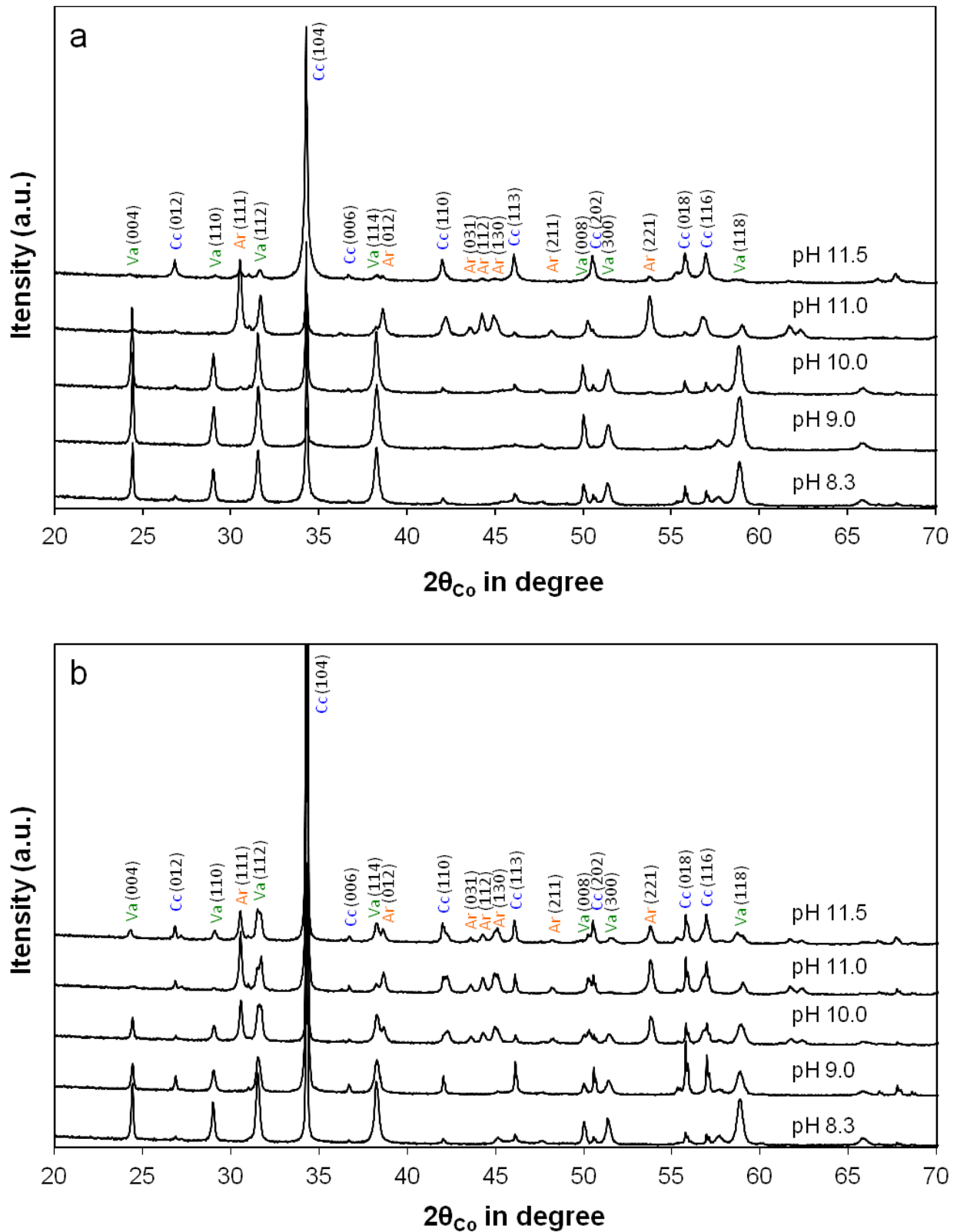


Fig. 4. Comparison of XRD pattern for (a) boron-free (#1-5) and (b) boron-containing experiments (#6-10) at pH 8.3, 9.0, 11.0 and 11.5 with **Cc** (calcite), **Ar** (aragonite) and **Va** (vaterite) indices. The characteristic peaks for the identification are $d_{104} = 3.04 \text{ \AA}$, $d_{111} = 3.39 \text{ \AA}$ and $d_{112} = 3.29 \text{ \AA}$ for calcite, aragonite and vaterite, respectively.

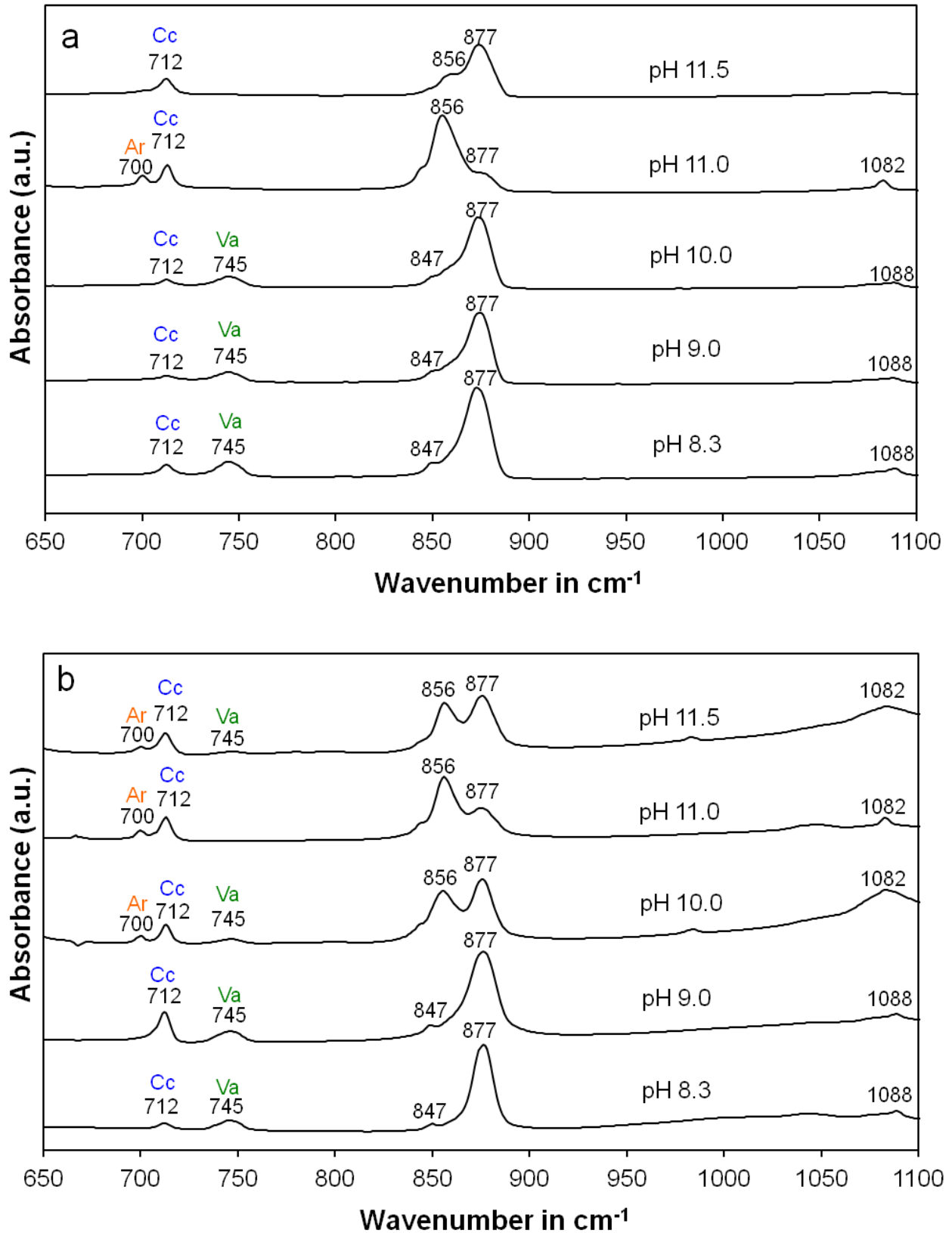


Fig. 5. Comparison of FTIR spectra for (a) boron-free (#1-5) and (b) boron-containing (#6-10) experiments at pH 8.3, 9.0, 10.0, 11.0 and 11.5 with characteristic Cc (calcite), Ar (aragonite) and Va (vaterite) peaks at 712 cm^{-1} for calcite, 700 and 712 cm^{-1} for aragonite and 745 cm^{-1} for vaterite.

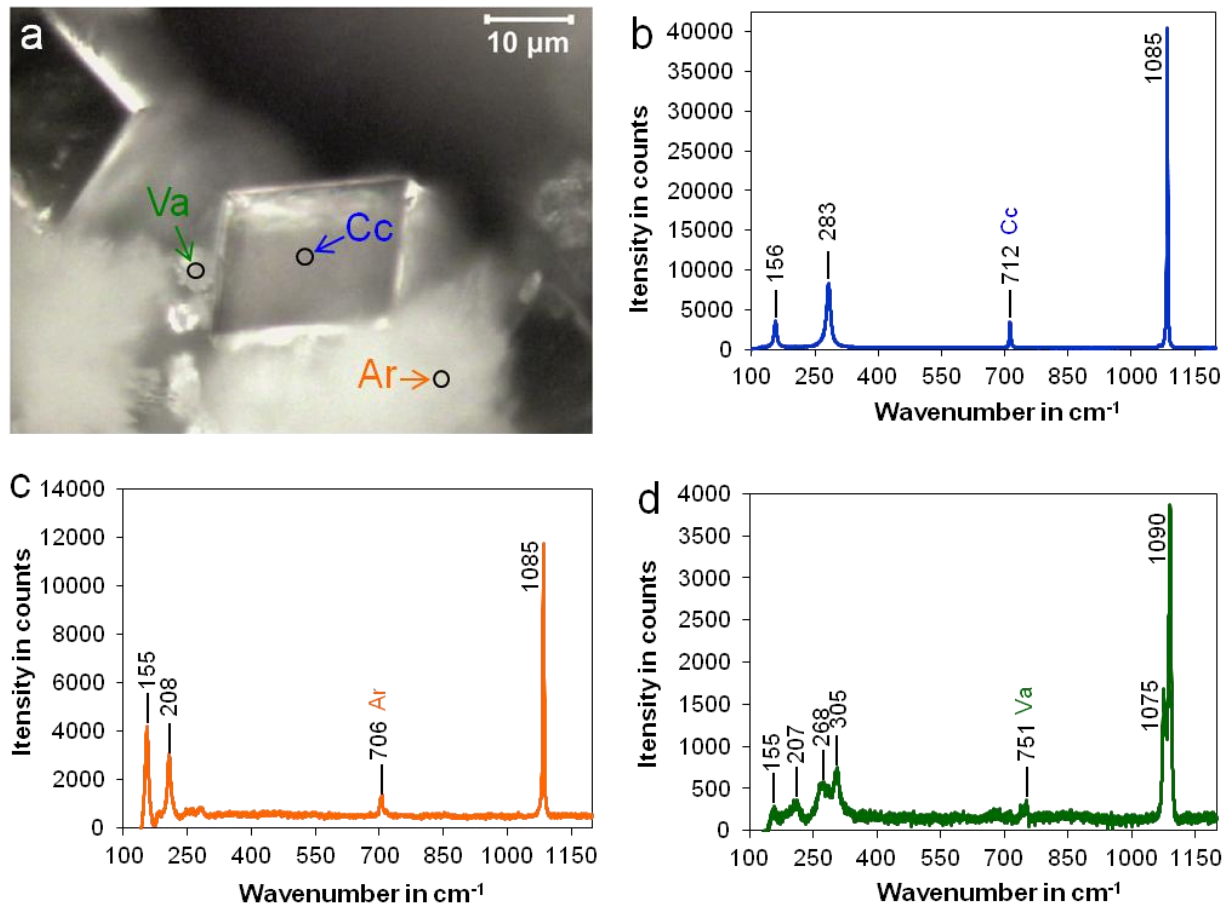


Fig. 6. (a) Characteristic image of analyzed calcite (Cc), aragonite (Ar) and vaterite (Va) of experiment pH 11.50 (#5) by Raman spectroscopy with a spot diameter of about 2 μm (black circle) and respective Raman spectra of (b) calcite, (c) aragonite and (d) vaterite with characteristic peaks at 712, 706 and 751 cm⁻¹, respectively.

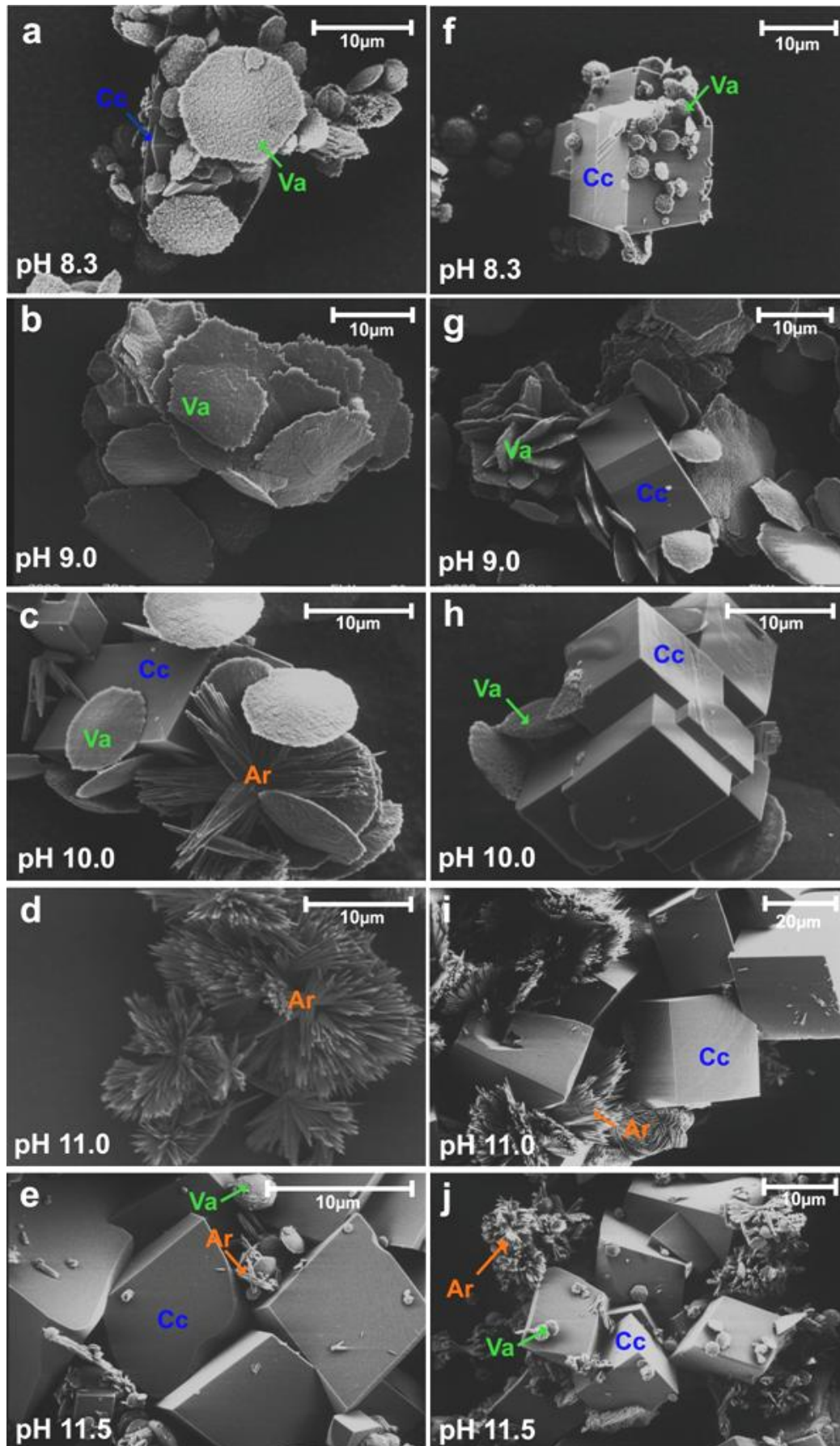


Fig. 7. SEM images of resulted precipitates from (a-e) boron-free (#1-5) and (f-j) boron-containing (#6-10) experiments. Cc: calcite, Va: vaterite, Ar: aragonite

Tab. 1. Experimental data for CO₂ diffusion experiments

Set	No.	T (°C)	pH	[B] mmol l ⁻¹	log UT _{CO2av} μmol h ⁻¹ l ⁻¹	log ACAR μmol h ⁻¹ l ⁻¹	t _{fc} h	log IAP _{fc}	t _g h	log R _{CaCO3} (III) μmol h ⁻¹ l ⁻¹	log R _{CaCO3} (IV) μmol h ⁻¹ l ⁻¹	log D _{Sr}	X _{Cc} wt. %	X _{Ar} wt. %	X _{Va} wt. %	Min
1	1	25	8.30	-	2.14	0.97	8.0	-7.44	7.3	2.85	1.96	-0.79	43	-	57	Va+Cc
	2	25	9.00	-	2.16	1.59	2.6	-7.27	15.3	2.52	2.00	-0.81	13	-	87	Va+Cc
	3	25	10.00	-	2.21	2.10	2.1	-6.95	20.1	2.21	1.96	-0.74	31	4	64	Va+Cc+Ar
	4	25	11.00	-	(2.32)	(2.31)	(0.5)	-	(20.0)	2.11	2.01	-0.09	10	87	2	Ar+Cc+Va
	5	25	11.50	-	(2.59)	(2.59)	(0.5)	-	(21.2)	2.11	2.01	-0.57	81	11	8	Cc+Ar+Va
2	6	25	8.30	0.42	2.13	0.96	8.5	-7.43	7.7	2.76	1.93	-0.80	38	-	62	Va+Cc
	7	25	9.00	0.40	2.19	1.62	2.2	-7.29	13.9	2.32	1.92	-0.75	39	-	61	Va+Cc
	8	25	10.00	0.43	2.17	2.06	1.1	-7.06	16.7	2.29	1.92	-0.30	15	37	48	Va+Ar+Cc
	9	25	11.00	0.41	(2.35)	(2.34)	(0.5)	-	(21.4)	2.10	2.00	-0.15	53	45	2	Cc+Ar+Va
	10	25	11.50	0.43	(2.46)	(2.46)	(0.5)	-	(19.3)	2.07	2.01	-0.35	53	36	11	Cc+Ar+Va

T: temperature; pH: pH of the outer solution; [B]: initial boron concentration; UT_{CO2av}: average uptake rate of CO₂ in the outer solution; ACAR: aqueous carbonate accumulation rate; t_{fc}: time of first net CaCO₃ precipitation; IAP_{fc}: ion activity product at t_{fc}; t_g: growth time of CaCO₃; R_{CaCO3}: overall precipitation rate of CaCO₃ in periods III and IV; D_{Sr}: distribution coefficient for Sr between aqueous solution and bulk CaCO₃; X_{Cc}, X_{Ar}, X_{Va}: fractions of calcite, aragonite and vaterite of the precipitate, respectively; Min: mineralogical composition of the precipitate listed in order of abundance; B/Ca: molar ratio of boron to calcium of the CaCO₃ precipitate; δ¹⁸O_{solid}: isotopic composition of the CaCO₃ precipitate; δ¹⁸O_{aq,0} and δ¹⁸O_{aq,f}: initial and final oxygen isotopic composition of the outer solution; 1000 · lnα_{calcite-water}: oxygen isotopic fractionation between calcite and water; s: slope of the regression line according to equation 23.

Set	No.	B/Ca μmol mol ⁻¹	δ ¹⁸ O _{solid} ‰ VPDB	δ ¹⁸ O _{aq,0} ‰ VPDB	δ ¹⁸ O _{aq,f} ‰ VPDB	10001 · nα _{calcite-water}	s
1	1	-	-10.52	-38.98	-38.98	29.18	-2.20
	2	-	-18.47	-39.08	-38.75	20.88	-2.22
	3	-	-25.56	-39.16	-39.24	14.14	-2.47
	4	-	-27.06	-39.27	-38.91	12.25	-4.03
	5	-	-27.49	-38.93	-39.11	12.02	-6.61
2	6	0.10	-10.69	-39.04	-39.14	29.18	-
	7	0.14	-19.27	-39.01	-39.17	20.50	-
	8	0.20	-25.23	-39.89	-39.11	14.34	-
	9	(0.15)	-27.91	-38.81	-39.12	11.60	-
	10	0.20	-27.15	-39.12	-38.95	12.20	-

4.2 Accumulation and Precipitation kinetics

4.2.1 First detection of CaCO_3 formation and crystal growth time

The obtained NaOH titration curves for experiments at pH 8.30, 9.00, 10.00, 11.00 and 11.50 (#1-5) are displayed in Figs. 8a to 12a, respectively. Obviously, the shapes of the titration curves differ from each other at distinct pH values. During period I the NaOH solution addition continuously balances the CO_2 uptake in the outer solution. The second period (II) is characterized by the time of first net CaCO_3 nucleation (t_{fc}), which was determined by the derivation of the NaOH titration curve (Fig. A2). The beginning of period III is defined by the intersection point of the regression lines A and B, which indicates - from now on - the dominance of CaCO_3 crystal growth vs. CO_2 uptake for the titration curve (t_g). In the last period (IV) the NaOH addition rate decreases in comparison with period III.

As seen by the titration curves of the experiments at pH 8.30, 9.00 and 10.00, the nucleation and thus first formation of CaCO_3 is detected by the minimum of the derivation of NaOH titration curve at experimental times of 8.3 ± 0.3 , 2.4 ± 0.2 and 1.6 ± 0.5 h, respectively. Obviously, period I becomes shorter and t_{fc} decreases with increasing pH. At $\text{pH} \geq 11.00$, CaCO_3 nucleation and precipitation starts almost instantaneously after adding the inner bag (CO_2 source) into the outer solution and t_{fc} cannot be obtained from the titration curve (see Fig. A3). Therefore, at pH 8.30, 9.00 and 10.00 the periods I and II can be determined (Figs. 8a, 9a and 10a), whereas at pH 11.00 and 11.50 the periods are not revealed (see Figs. 11a and 12a). Consequently, period III, the dominant precipitation stage is reached earlier at elevated pH. The decrease of time periods I and II is related to an elevated overall time periods of CaCO_3 crystal growth (periods III and IV) within the duration of the whole experiment. For instance, a pH of 8.30 and 10.00 (#1 and #3) result in $t_g = 7.3$ and 20.1 h, respectively. At $\text{pH} \geq 11.00$ t_g is approximated by the total experimental time. The values of t_{fc} and t_g of all experiments are given in Tab. 1. At pH 8.30 the precipitation periods III and IV can obviously be followed by the elevated amounts of added NaOH (Fig. 8a). However, periods III and IV can be less precise quoted at higher pH (Fig. 12a).

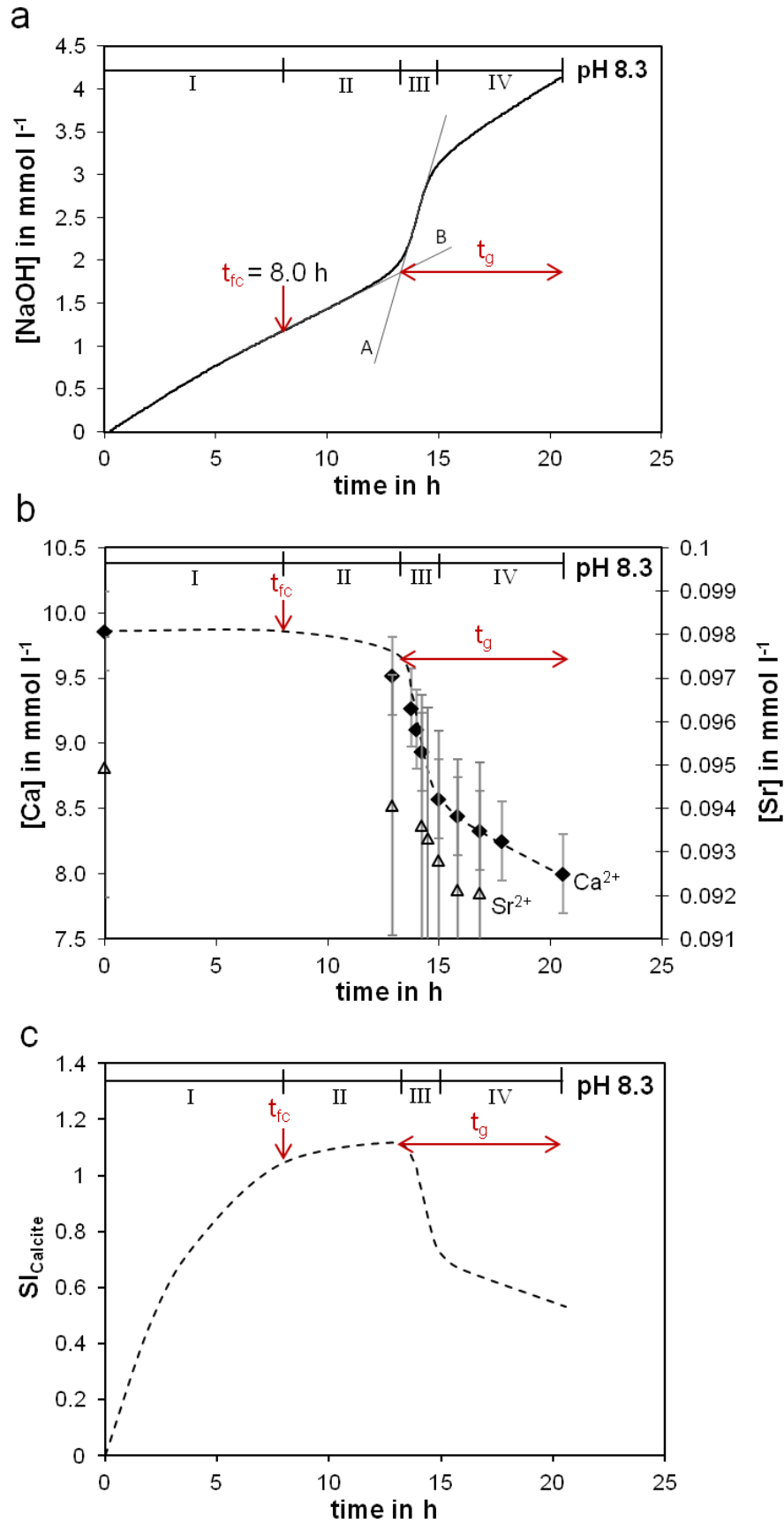


Fig. 8. Evolution of (a) NaOH addition, (b) Ca^{2+} and Sr^{2+} concentrations and (c) saturation index with respect to calcite, SI_{calcite} , of the outer solution during the experimental run time at pH 8.30 (#1). t_{fc} and t_g denote the time for the detection of first net CaCO_3 nucleation and the CaCO_3 crystal growth time during periods III and IV, respectively. \blacklozenge : measured $[\text{Ca}]$ by IC; dashed line: estimated $[\text{Ca}]$ and SI_{calcite} by NaOH titration data.

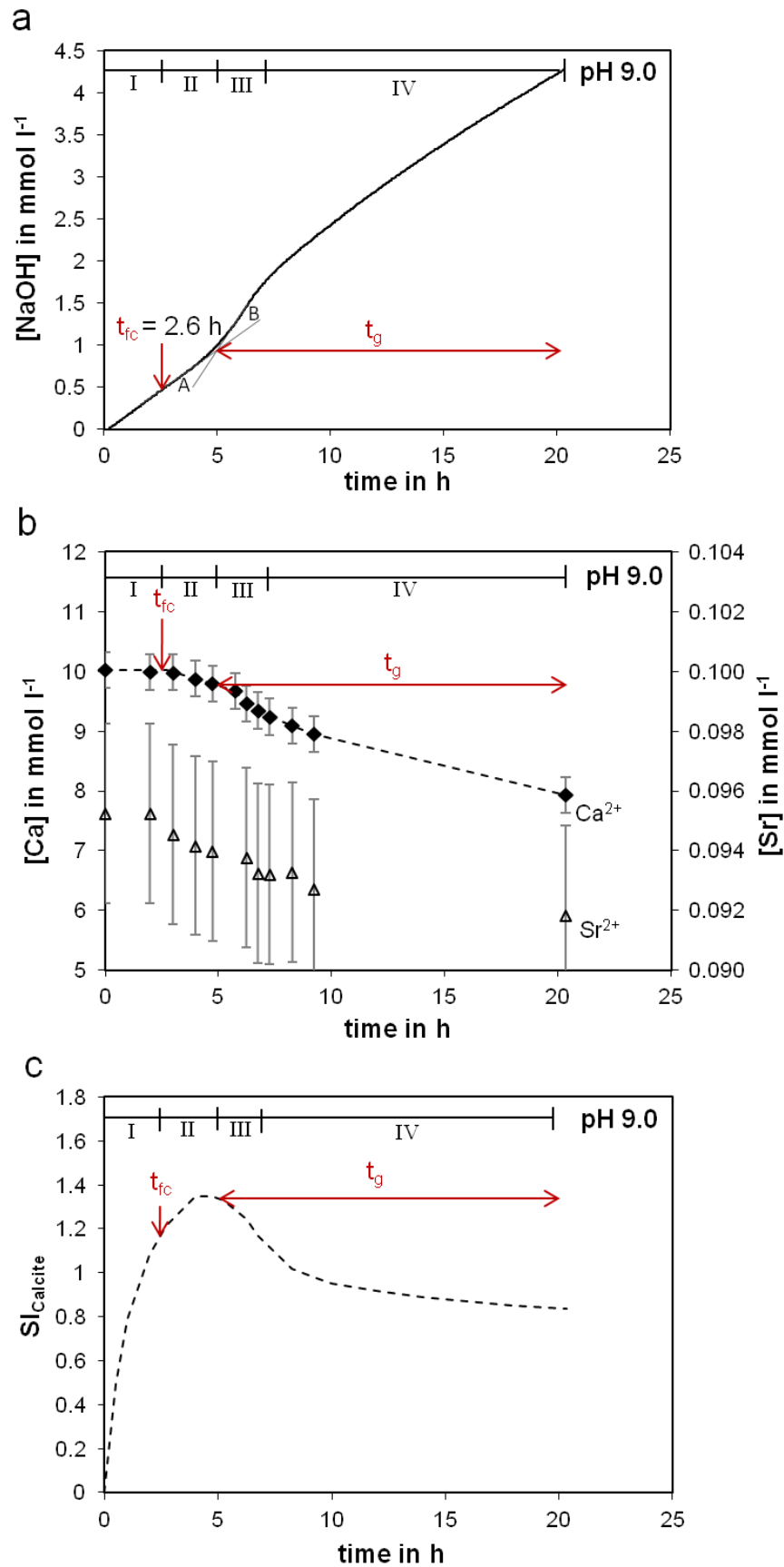


Fig. 9. Evolution of (a) NaOH addition, (c) Ca²⁺ and Sr²⁺ concentrations and (b) saturation index with respect to calcite, SI_{calcite} , of the outer solution during the experimental time run at pH 9.00 (#2). t_{fc} and t_g denote the time for the detection of first net CaCO₃ nucleation and the CaCO₃ crystal growth time during periods III and IV, respectively. ♦: measured [Ca] by IC; dashed line: estimated [Ca] and SI_{calcite} by NaOH titration data.

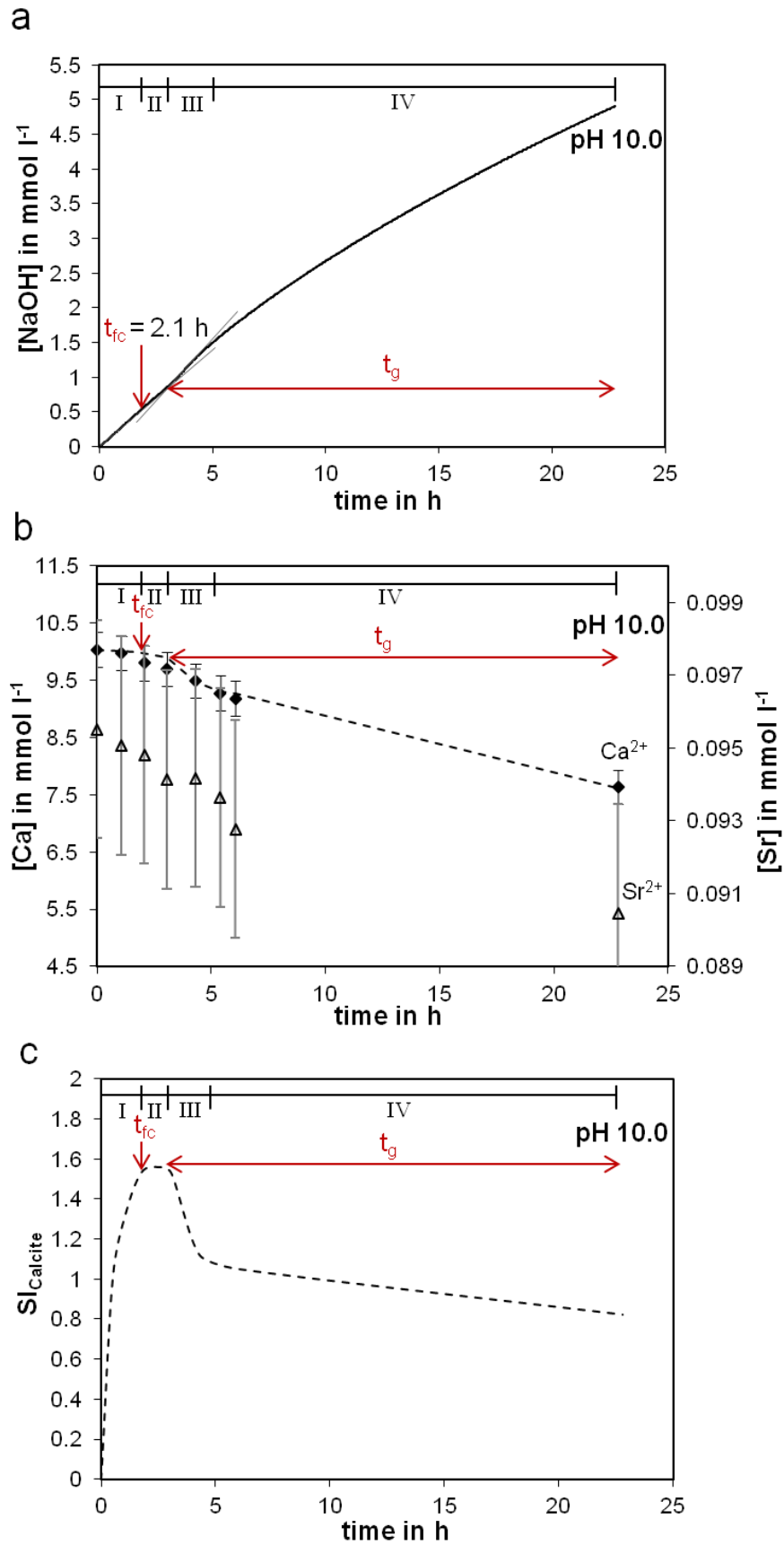


Fig. 10. Evolution of (a) NaOH addition, (c) Ca^{2+} and Sr^{2+} concentrations and (b) saturation index with respect to calcite, SI_{calcite} , of the outer solution during the experimental time run at pH 10.00 (#3). t_{fc} and t_g denote the time for the detection of first net CaCO_3 nucleation and the CaCO_3 crystal growth time during periods III and IV, respectively. \blacklozenge : measured $[\text{Ca}]$ by IC; dashed line: estimated $[\text{Ca}]$ and SI_{calcite} by NaOH titration data.

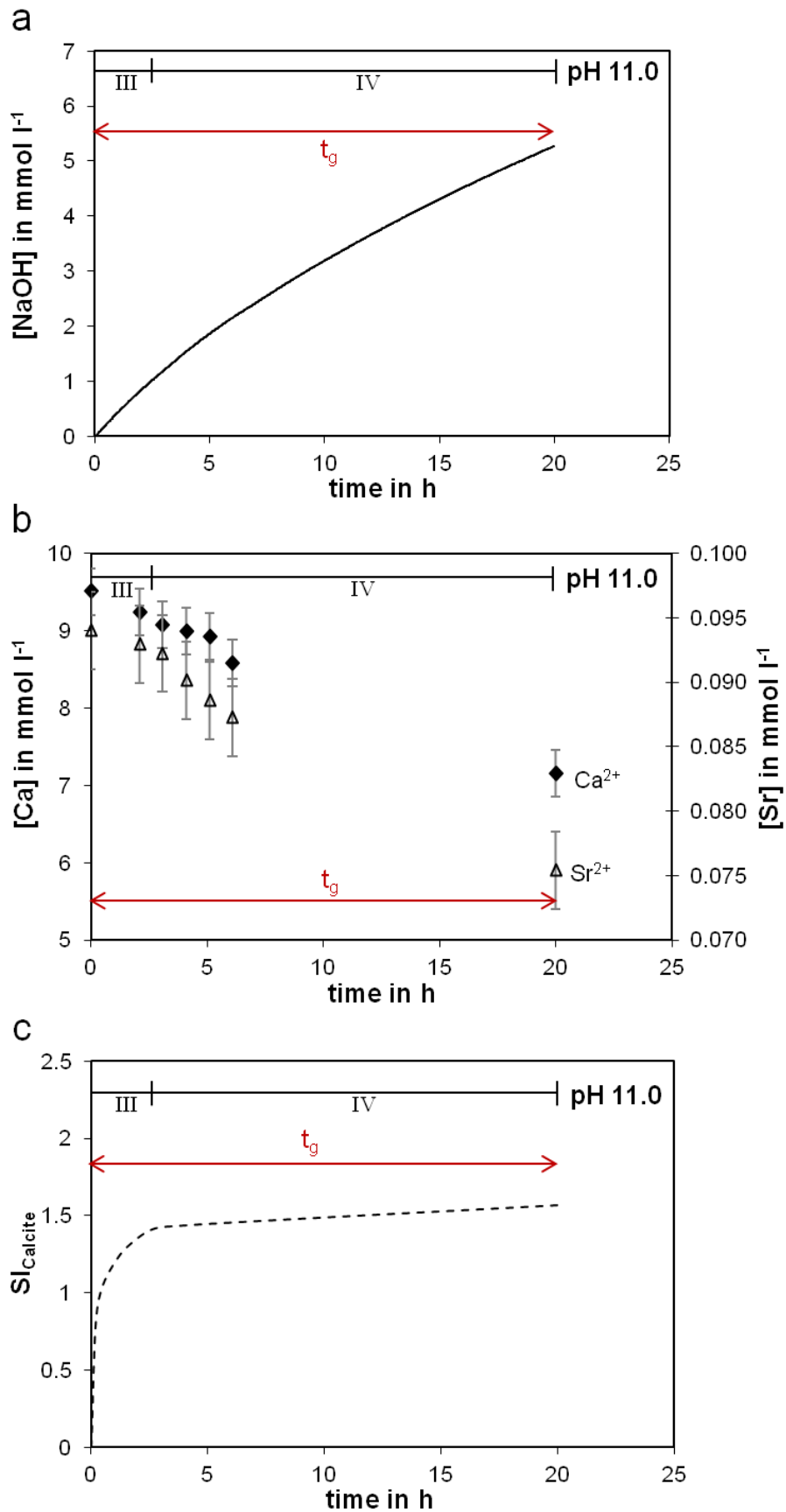


Fig. 11. Evolution of (a) NaOH addition, (c) Ca²⁺ and Sr²⁺ concentrations and (b) saturation index with respect to calcite, SI_{calcite} , of the outer solution during the experimental time run at pH 11.00 (#4). t_g denotes the CaCO₃ crystal growth time. ♦: measured [Ca] by IC; dashed line: estimated SI_{calcite}

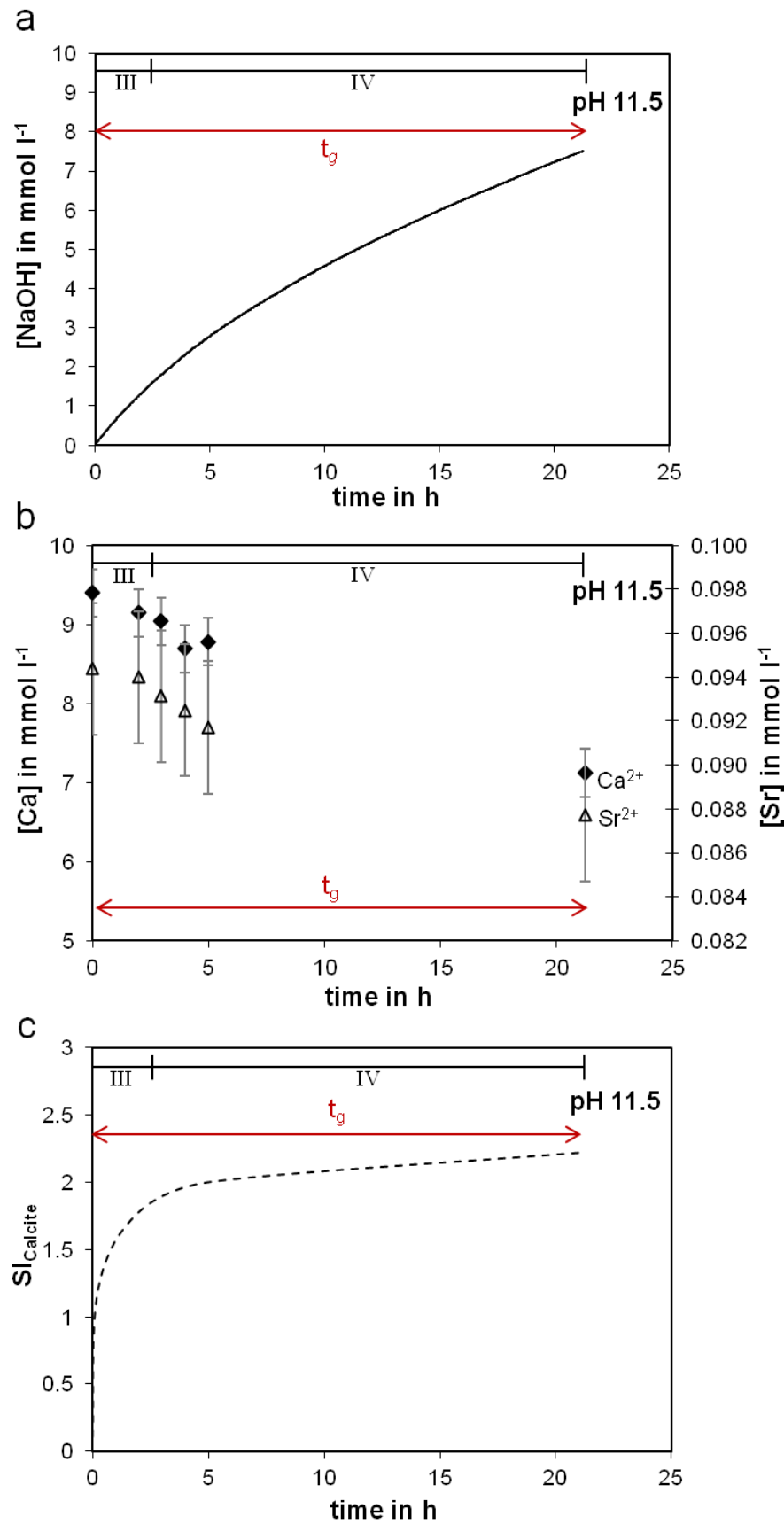


Fig. 12. Evolution of (a) NaOH addition, (c) Ca²⁺ and Sr²⁺ concentrations and (b) saturation index with respect to calcite, SI_{calcite}, of the outer solution during the experimental time run at pH 11.50 (#5). t_g denotes the CaCO₃ crystal growth time. ♦: measured [Ca] by IC; dashed line: estimated SI_{calcite}

4.2.2 CO₂ uptake and aqueous carbonate accumulation rate

The UT_{CO_2av} and ACAR calculated for period I according to equations 16 and 17, respectively, are given in Tab. 1. As mentioned before, period I could not be determined by the titration curves of experiments at $pH \geq 11.00$. In the latter case the UT_{CO_2av} and ACAR values were referred to $t_{fc} = 0.5$ h, as it can be reasonable suggested that the decrease of Ca^{2+} concentration was of limiting influence for the calculation of these parameters at this initial stage (see Figs. 11b and 12b). The effect of pH on UT_{CO_2av} and ACAR is displayed in Figs. 13a and 13b, respectively (average values of sets 1 and 2). At elevated pH of the outer solution the UT_{CO_2av} and the ACAR values are significantly higher compared to lower pH conditions. For instance pH 8.30 results in an ACAR of $9.2 \pm 0.1 \mu\text{mol h}^{-1} \text{ l}^{-1}$, whereas ACAR = $121 \pm 6 \mu\text{mol h}^{-1} \text{ l}^{-1}$ is significantly higher at pH 10.00.

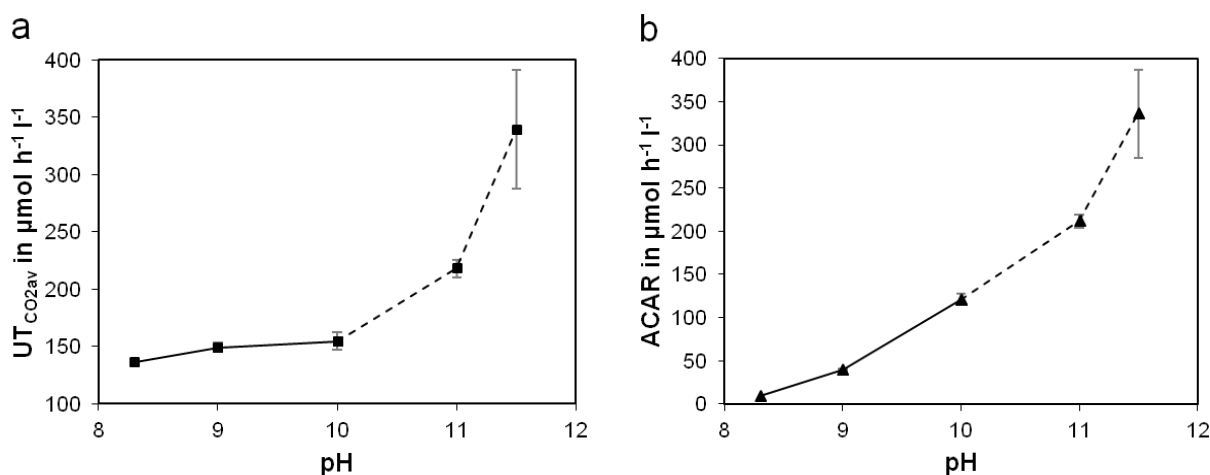


Fig. 13. Average (a) UT_{CO_2av} and (b) ACAR values of the experiments (#1-10) versus pH. UT_{CO_2av} is the average uptake rate of CO₂ and ACAR the aqueous carbonate accumulation rate in the outer solution.

4.2.3 Precipitation rate of CaCO₃

The evolution of the analyzed [Ca] values during the experimental run time is displayed in Figs. 8b to 12b for experiments at pH 8.30, 9.00, 10.00, 11.00 and 11.50 (#1-5), respectively. The overall precipitation rate of CaCO₃ (R_{CaCO_3}) was calculated according to equation 18 by considering the measured [Ca] of the outer solution in periods III and IV (see Tab. 1). The R_{CaCO_3} values are based on [Ca], which is consumed during the precipitation of the bulk CaCO₃ comprising individual fractions of calcite, aragonite and vaterite (see X_{Cc} , X_{Ar} and X_{Va} in Tab. 1).

Obviously, R_{CaCO_3} values are significantly higher at low versus high pH in period III (Fig. 14a). In the dominant precipitation period III calculations at pH 8.30 (#1) and 10.00 (#3) result in $R_{\text{CaCO}_3} = 710$ and $162 \mu\text{mol h}^{-1} \text{ l}^{-1}$, respectively. However, compared to period III the R_{CaCO_3} values are considerably lower in the subsequent precipitation period IV. For instance at pH 9.00 (#2) periods III and IV result in $R_{\text{CaCO}_3} = 328$ and $100 \mu\text{mol h}^{-1} \text{ l}^{-1}$, respectively. The difference between the precipitation rates within periods III and IV decreases with increasing pH. At $\text{pH} \geq 11.00$ the difference between the periods can be barely resolved (at pH 11.00 (#4) periods III and IV result in $R_{\text{CaCO}_3} = 128$ and $103 \mu\text{mol h}^{-1} \text{ l}^{-1}$, respectively). Interestingly, the obtained R_{CaCO_3} values within period IV are very similar for all experiments independently on pH ($94 \pm 10 \mu\text{mol h}^{-1} \text{ l}^{-1}$, see Tab. 1). The relative [Ca] decrease (equivalent to the amount of precipitated CaCO_3) was similar ($22 \pm 4 \text{ mol}\%$ in respect to initial Ca^{2+} concentrations) for all experiments by reaching the total experimental time of about 20 h (Fig. 14b).

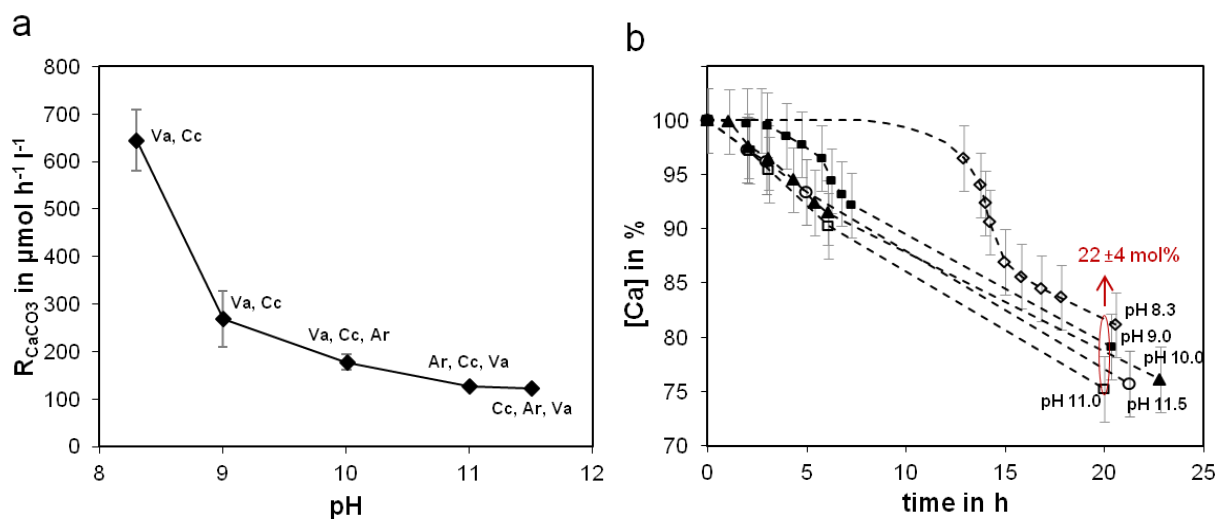


Fig. 14. (a) Average overall precipitation rate of CaCO_3 , R_{CaCO_3} , within period III of experiments (#1-10) versus pH, where precipitated CaCO_3 polymorphs are given: calcite (Cc), vaterite (Va) and aragonite (Ar). (b) Relative decrease of the Ca^{2+} concentration in respect to initial Ca^{2+} content during the whole experimental runs (#1-5).

4.2.4 Recalculation of UT_{CO_2}

Beside the chemical analysis of the [Ca] values of the outer solution during the experimental time, the evolution was also modeled throughout the titration curve by equation 19. In Fig. 15a the evolution of analyzed and modeled [Ca] values are compared for pH 8.30 (#1). Obviously, the values of the modeled and measured [Ca] differ from each other with increasing time. This behavior is valid for all experiments. The modeled Ca^{2+} concentrations were derived by considering a constant UT_{CO_2} ($UT_{\text{CO}_2\text{av}}$). It can be reasonable assumed that

the latter factor is changing throughout the experiments as the slope of titration curve within the period I slightly decreases as a function of experimental time (see Fig. 8a). Based on the results of the measured $[Ca]$ values the $NaOH_{CO_2}$ addition rates and the UT_{CO_2} were recalculated. As seen in Fig. 15b the obtained apparent current UT_{CO_2} ($UT_{CO_2,ti}$) continuously decreases during the experimental run time. Beyond the experimental time t_{fc} the relationship between the UT_{CO_2av} and the experimental time can be described by the following linear function

$$UT_{CO_2,ti} = s \cdot (t_i - t_{fc}) + UT_{CO_2av} \quad (23)$$

for individual pH values, where UT_{CO_2av} is the average overall CO_2 uptake rate according to equation 19 and $UT_{CO_2,ti}$ is the re-calculated current CO_2 uptake rate at a certain time step (t_i) during the experiment (s values are given in Tab. 1). Based on the individual $UT_{CO_2,ti}$ the $[Ca]$ values were aligned accordingly. As seen in Fig. 15a (#1) the difference between the measured and modeled $[Ca]$ values could be compensated by considering the above continuously decrease of the $UT_{CO_2,ti}$ values.

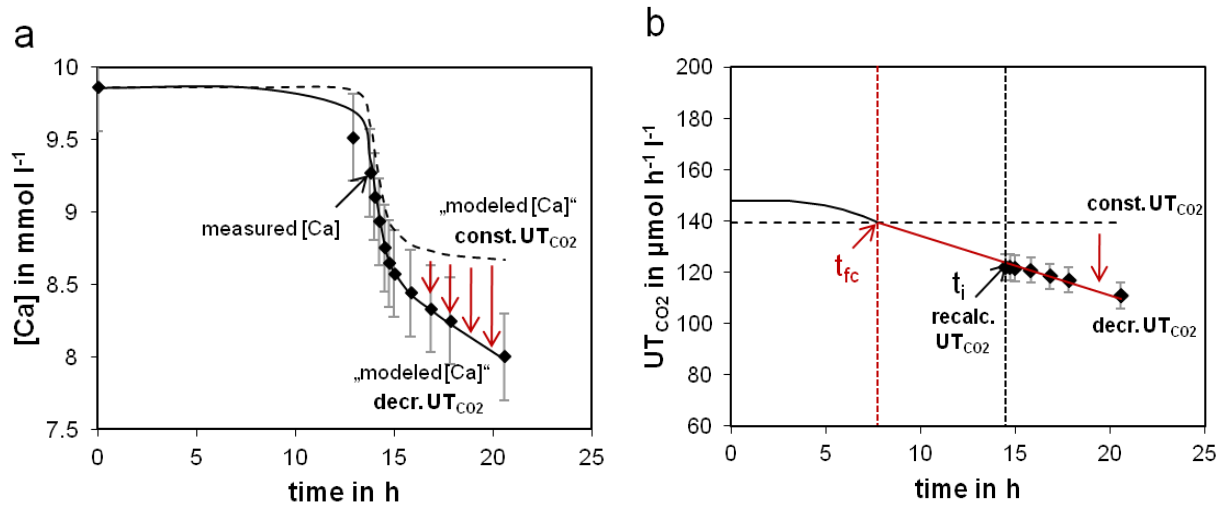


Fig. 15. (a) Comparison of measured and modeled $[Ca]$ by assuming a constant (dashed line) and decreasing (solid line) CO_2 uptake rate (UT_{CO_2av}) of the experiment at pH 8.30 (#1). (b) Constant UT_{CO_2av} (dashed line) and re-calculated $UT_{CO_2,ti}$ (black symbols) by considering the measured $[Ca]$ at pH 8.3 (#1). Beyond the time of detection of net $CaCO_3$ nucleation, t_{fc} , the $UT_{CO_2,ti}$ decreases with experimental run time according to equation 23.

The $[Ca]$ values were also aligned for pH 9.00 and 10.00 accordingly (see Figs. 9b and 10b). At $pH \geq 11.00$ aqueous CO_3^{2-} dominates the DIC in the outer solution and small amounts of NaOH solution are added during the precipitation of $CaCO_3$. Therefore, the $[Ca]$ values

cannot be modeled precisely throughout the titration curve and the modeled evolution of Ca^{2+} decrease is not given in Figs. 11b and 12b.

4.2.5 Ion activity product for CaCO_3 and saturation index with respect to calcite

The ion activity product ($\text{IAP} = (\text{Ca}) \cdot (\text{CO}_3)$) and saturation index with respect to calcite were modeled by considering the pH, the analyzed solution chemistry and the DIC content of the outer solution. The DIC content was calculated by the $\text{UT}_{\text{CO}_2, \text{ti}}$, which is equal to the DIC uptake rate in the outer solution, considering the consumed CO_3^{2-} ions through CaCO_3 precipitation (R_{CaCO_3} value). A decrease of $\text{UT}_{\text{CO}_2, \text{ti}}$ is obtained during the experimental time by using individual equations 23 (see Fig. 15b). The modeled IAP values at the time of first net nucleation, IAP_{tfc} , are given in Tab. 1 for all experiments. At t_{fc} higher IAP values are reached at elevated pH, e.g. pH 8.30 (#1) and 10.00 (#3) result in $\log(\text{IAP}_{\text{tfc}})$ of -7.44 and -6.95, respectively. The evolution of SI with respect to calcite, $\text{SI}_{\text{calcite}}$, over time is displayed for individual experiments at pH 8.30, 9.00, 10.00, 11.00 and 11.50 in Figs. 8c to 12c, respectively. The values of $\text{SI}_{\text{calcite}}$ continuously increase until t_{fc} is reached. Subsequently, the $\text{SI}_{\text{calcite}}$ increases - but less strongly as before - until period III, the dominant precipitation stage, is reached. In periods III and IV the growth of CaCO_3 crystals lead to a decrease of $\text{SI}_{\text{calcite}}$ until the end of the experiment. This behavior is only valid for experiments at $\text{pH} \leq 10.00$ (Figs. 8c to 10c). In contrast, in the experiments at $\text{pH} \geq 11.00$ the $\text{SI}_{\text{calcite}}$ is not decreasing, but increases slightly during the whole experiment (Figs. 11c and 12c). It has to be kept in mind that the CaCO_3 precipitates in the present experiments consist of Cc, Va and Ar, depending on pH. However, the evolution of the respective SI values (and IAP values) is identical to that of $\text{SI}_{\text{calcite}}$, if the individual solubility constants are considered.

4.3 Coprecipitation of Sr and B with CaCO_3

4.3.1 Sr coprecipitation

The coprecipitation of Sr with CaCO_3 precipitation can be followed by the overall distribution coefficient, D_{Sr} , which was determined by equation 10 (see values in Tab. 1). The D_{Sr} values of the individual experiments were calculated by plotting $\log \{([\text{Sr}]/[\text{Ca}])_{\text{aq}}/([\text{Sr}]/[\text{Ca}]_{\text{aq},0})\}$ vs. $\log \{([\text{Ca}]_{\text{aq}}/[\text{Ca}]_{\text{aq},0})\}$, where the slope is referred to ($D_{\text{Sr}} - 1$) (Fig. 16).

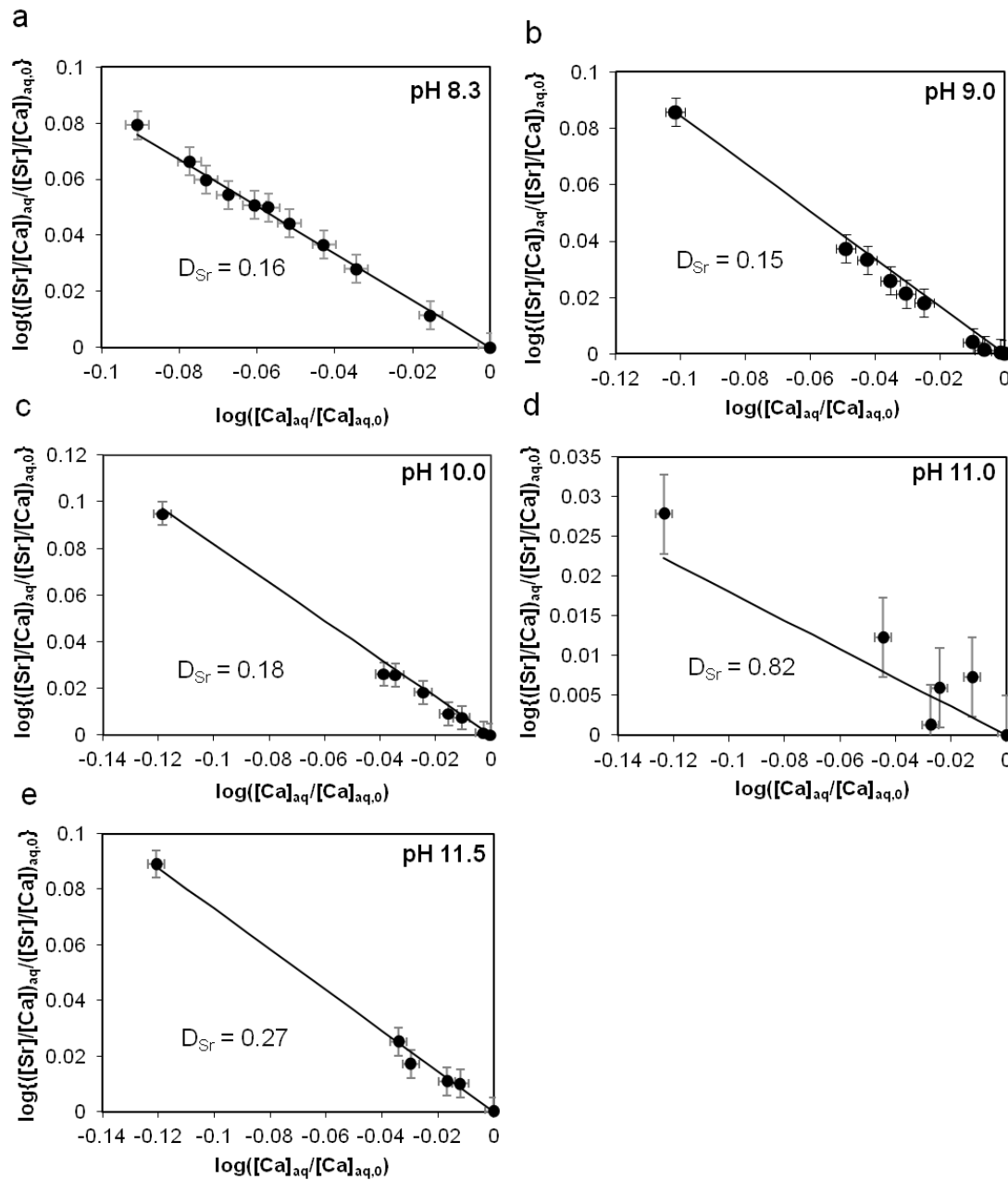


Fig. 16. Characteristic plots of $\log\{([\text{Sr}]/[\text{Ca}])_{\text{aq}}/([\text{Sr}]/[\text{Ca}]_{\text{aq},0})\}$ vs. $\log\{([\text{Ca}]_{\text{aq}}/[\text{Ca}]_{\text{aq},0})\}$ for the experiments #1-5 at the given pH values (solid cycles denote experimental data). The solid line represents the linear regression of the experimental data with a slope of ($D_{\text{Sr}} - 1$) (see equation 10).

The highest D_{Sr} values are reached in experiments at pH 11.00 (#4 and #9 with $D_{Sr} = 0.82$ and 0.70, respectively). This is related to a strong decrease of $[Sr]/[Ca]$ ratio in the aqueous solution and a lower slope in Fig. 16d. In contrast, the D_{Sr} values are much lower at $pH \leq 9.0$ with an average D_{Sr} of 0.16 ± 0.01 documented by a higher slope of the regression lines in Figs. 16a and 16b.

4.3.2 B coprecipitation

The obtained B/Ca ratios (in $\mu\text{mol mol}^{-1}$) of the bulk CaCO_3 precipitates of the second set (#6-10) are given in Tab. 1. The relation between the B/Ca ratio and the pH of the outer solution is displayed in Fig. 17. Obviously, the B/Ca ratio increases from pH 8.30 to 10.00. At $pH \geq 10.00$ the ratio remains almost constant, except for pH 11.00 (#9) (possible failure in preparation for analyses).

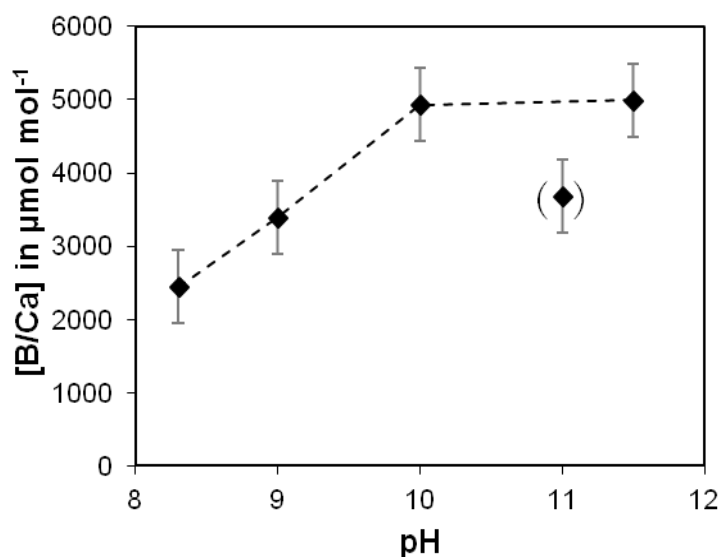


Fig. 17. B/Ca ratios of the bulk CaCO_3 precipitates (#6-10) versus pH. (): experiment #9 is not considered for the connecting line due to an assumed preparation failure.

4.4 Stable oxygen isotopes

The $\delta^{18}\text{O}$ values of analyzed bulk CaCO_3 precipitates and solutions are given in Tab. 1 for all experiments. The average $\delta^{18}\text{O}$ value for H_2O is -39.1 ± 0.1 ‰ (VPDB) considering both the initial and final outer solutions. Thus, no change of isotopic composition is observed during all experimental runs. The relationship between the $\delta^{18}\text{O}$ values of measured received solids (bulk CaCO_3) and the pH is displayed in Fig. 18. It is obvious that isotopically lighter CaCO_3 is favorably formed at elevated pH. Calcium carbonates precipitated at pH 8.30 show an average $\delta^{18}\text{O}$ value of -10.6 ± 0.1 ‰ (VPDB), whereas at pH 11.00 and 11.50 an average $\delta^{18}\text{O}$ value of -27.4 ± 0.3 ‰ (VPDB) is obtained.

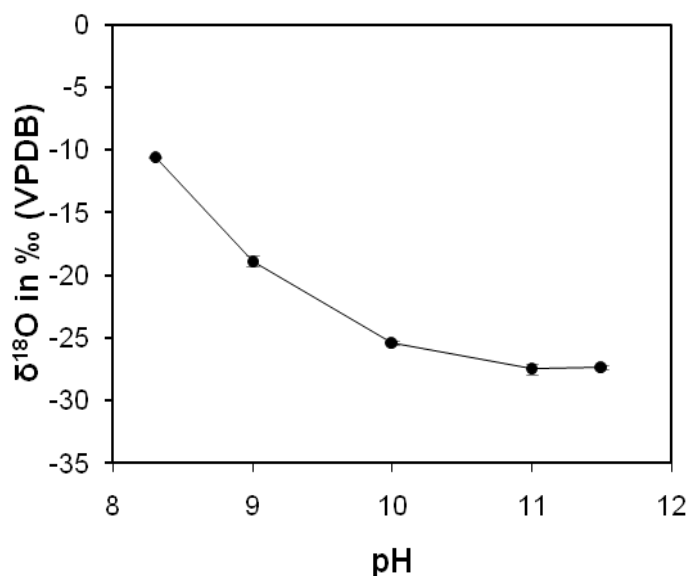


Fig. 18. Average $\delta^{18}\text{O}$ values of bulk CaCO_3 versus pH (#1-10).

The oxygen isotopic fractionation factor ($\alpha_{\text{calcite-water}}$) between calcite and water was calculated according to equation 12 for all experiments. The results are given as $1000 \cdot \ln \alpha_{\text{calcite-water}}$ values in Tab. 1. Obviously, the $1000 \cdot \ln \alpha_{\text{calcite-water}}$ values are lower at elevated pH compared to lower pH conditions (e.g. pH 8.30 (#1) and 11.50 (#5) result in $1000 \cdot \ln \alpha_{\text{calcite-water}}$ of 29.2 and 12.0 ‰, respectively).

5. DISCUSSION

5.1 Uptake rate of CO₂

The UT_{CO_2av} value of the outer solution depends on the thickness of the given PE membrane (constant: 0.2 mm) and on the CO₂ partial pressure gradient between the inner and the outer solution. The initially adjusted P_{CO_2} of the inner solution is in all experiments $P_{CO_2} = 10^{-0.20}$ atm, but is slightly changing throughout the experiments due to the loss of CO₂ by the diffusion through the membrane. Recalculation of the P_{CO_2} of the inner solution by the total uptake of CO₂ in the outer solution results in $P_{CO_2} = 10^{-0.37}$, $10^{-0.37}$, $10^{-0.39}$, $10^{-0.40}$ and $10^{-0.43}$ atm at the end of the experiments for pH 8.30, 9.00, 10.00, 11.00 and 11.50, respectively. In contrast, as soon as gaseous CO₂ is liberated into the outer solution its P_{CO_2} depends on the adjusted pH between 8.30 and 11.50. At elevated pH of the outer solution the P_{CO_2} is significant lower compared to lower pH conditions due to the individual distribution of DIC species. Therefore, the UT_{CO_2av} of the outer solution increases with rise in pH stimulated by an increase of the CO₂ partial pressure gradient between the inner and outer solution.

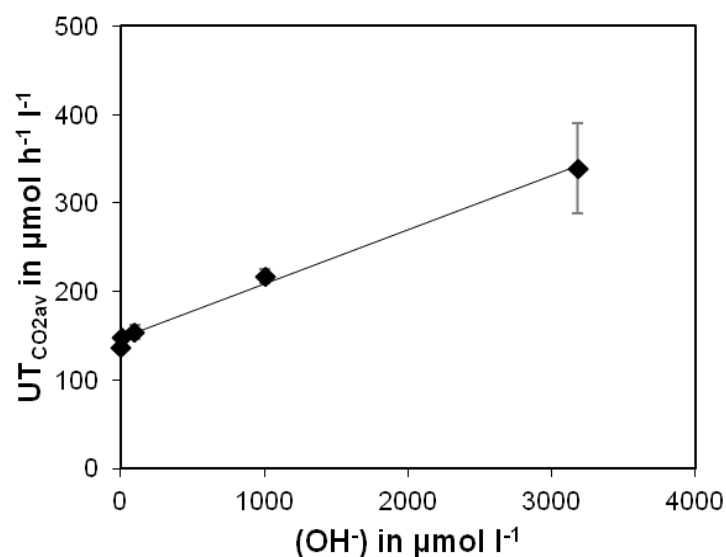
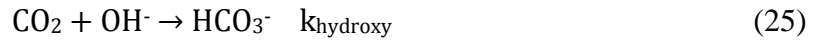


Fig. 19. Average CO₂ uptake rates (UT_{CO_2av}) of experiments (#1-10) versus the activity of OH⁻ (in $\mu\text{mol L}^{-1}$) of the outer solution.

Fig. 19 shows a linear relationship between the activity of OH⁻ in the outer solution and the UT_{CO_2av} values of sets 1 and 2 according to the equation

$$UT_{CO_2av} = 0.062 \cdot (OH^-) + 147 \quad (24)$$

which is in particular valid for $\text{pH} \geq 9$. The higher the (OH^-) , the higher the $\text{UT}_{\text{CO}_2\text{av}}$ value is. In alkaline solutions CO_2 hydroxylation besides hydration occurs. Thus, at $\text{pH} \geq 9$ the received CO_2 molecule preferentially reacts according to the reaction



where HCO_3^- partially yields in CO_3^{2-} by deprotonation depending on pH . In our experiments at $\text{pH} \geq 9$ with high P_{CO_2} gradients between inner and outer solutions an almost unidirectional uptake reaction (25) can be reasonable assumed throughout the experiments. The individual CO_2 hydroxylation kinetics can be expressed by

$$-\frac{d[\text{CO}_{2(\text{aq})}]}{dt} = k_{\text{hydroxy}} \cdot [\text{OH}^-] \cdot [\text{CO}_{2(\text{aq})}] \quad (26)$$

($k_{\text{hydroxy}} = 10^{3.93} \text{ l mol}^{-1} \text{ s}^{-1}$ at 25°C ; Usdowski, 1982).

Fig. 20 shows the correlation of the $\text{UT}_{\text{CO}_2\text{av}}$ values with the concentration of aqueous CO_2 , which had reacted with OH^- according to equation 26 at 60 seconds. At elevated pH the transferred CO_2 in the outer solution reacts instantly with OH^- to HCO_3^- (reaction 25) and dissociates to CO_3^{2-} . Thus, the P_{CO_2} of the outer solution at higher pH is significant lower compared to lower pH conditions.

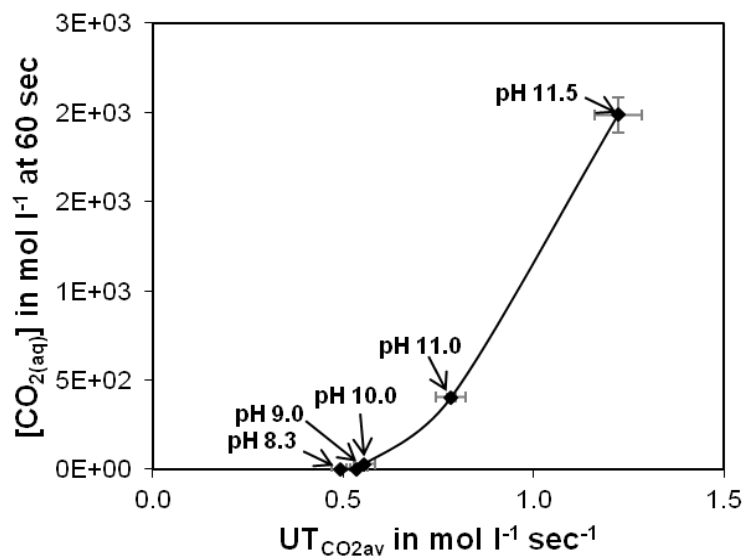


Fig. 20. Average CO_2 uptake rates ($\text{UT}_{\text{CO}_2\text{av}}$) of experiments (#1-10) versus the concentration of aqueous CO_2 at 60 sec according to equation 26.

As mentioned before the P_{CO_2} of the inner solution is slightly decreasing throughout the experiments due to the loss of CO_2 by diffusion through the membrane. This is also shown in the continuously decrease of the obtained $UT_{\text{CO}_2\text{av}}$ during the experimental run time (see Fig. 15b). The relationship between the $UT_{\text{CO}_2\text{,ti}}$ and the experimental time according to equation 23 yields in elevated slopes at elevated pH conditions (see s -values in Tab. 1). This means that the $UT_{\text{CO}_2\text{,ti}}$ decreases faster over experimental time at elevated pH compared to lower pH conditions. This can be explained by the elevated loss of CO_2 (DIC) of the inner solution (see Fig. 21) due to significant higher UT_{CO_2} values at elevated pH.

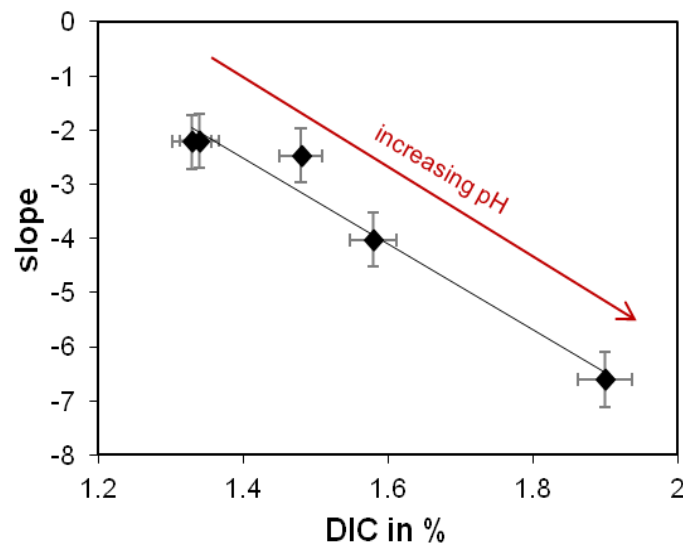


Fig. 21. Loss of dissolved inorganic carbon (DIC) of the inner solution by CO_2 diffusion through the PE membrane in % versus the slope from equation 23 for experiments at pH 8.30 to 11.50 (#1-5) (s -values are given in Tab. 1).

5.2 Aqueous carbonate accumulation rate

High vs. low pH result in elevated ACAR due to (i) a higher P_{CO_2} gradient between the inner and outer solution, (ii) the dominance of CO_2 hydroxylation reaction, and (iii) elevated $[\text{CO}_3^{2-}]/[\text{DIC}]$ ratios at high pH. Throughout the experiments the IAP ($= (\text{Ca}^{2+}) \cdot (\text{CO}_3^{2-})$) of the outer solution increases by the continuous accumulation of CO_3^{2-} more rapidly at higher vs. lower pH. Consequently, less overall experimental time for CaCO_3 nucleation is required compared to lower pH conditions and t_{fc} - monitored by titration curves - is reached earlier. The obtained t_{fc} and ACAR values of the present study were plotted in Fig. 22 with the data from Niedermayr et al. (2013), who carried out analogous experiments by using the CO_2 diffusion technique, but with two PE membrane thickness at pH 8.30 (25°C). Our t_{fc} - ACAR relationship correlates well with the values from Niedermayr et al. (2013) at pH 8.30.

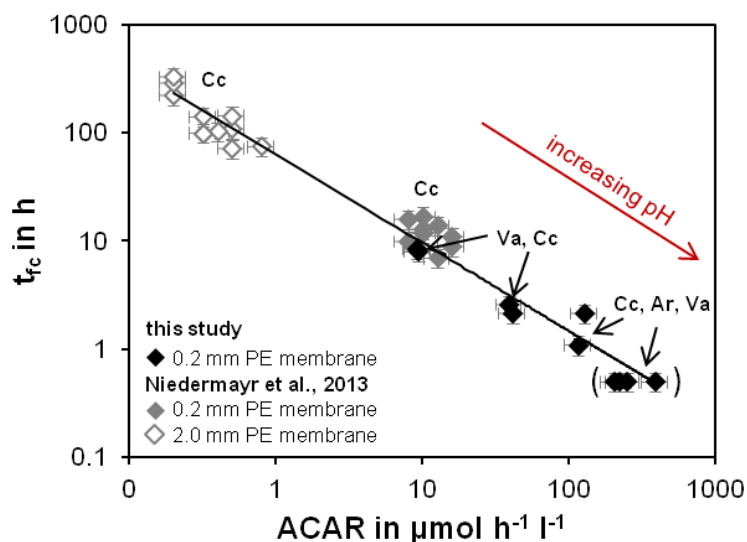


Fig. 22. Aqueous carbonate accumulation rate, ACAR, versus the time for the first detection of net CaCO_3 nucleation, t_{fc} , of the experiments (25°C) from the present study and from Niedermayr et al. (2013). (): experiments at $\text{pH} \geq 11$ (#4-5, #9-10), where $t_{\text{fc}} = 0.5$ h was assessed.

A thicker PE membrane results in significant lower $UT_{\text{CO}_2\text{av}}$ and ACAR values and the CaCO_3 precipitation is delayed (open diamonds in Fig. 22). Beside the thickness of the PE membrane the pH of the outer solution is another important factor, which influences the ACAR and consequently t_{fc} . An increase in pH causes higher ACAR and lower t_{fc} values at a given PE membrane (black diamonds). The t_{fc} value does obviously not depend on the formation of distinct CaCO_3 polymorphs. Interestingly, the combined data obtained by the change of

membrane thickness and/or changing pH yields a strong negative correlation according to the equation

$$\log (t_{fc}) = -0.82 \cdot \log (ACAR) + 1.80 \quad (27)$$

Thus, the t_{fc} is highly controlled by the ACAR, which can be adjusted by both membrane type and pH.

5.3 *CaCO₃ nucleation and growth*

During the experimental run aqueous CO_3^{2-} ions accumulate continuously in the outer solution through the uptake, hydration and hydroxylation of CO_2 and subsequent dissociation reactions. The IAP threshold for the net CaCO_3 nuclei formation in the outer solution is appointed by an inflection point of the titration curve of experiments at $\text{pH} \leq 10.00$ (see borderline between periods I and II in Fig. A2 for $\text{pH} 8.30$). Although, CaCO_3 is formed, the IAP with respect to CaCO_3 (or saturation index in respect to individual polymorphs) continues to increase - but less strongly as before - until the end of period II, where a maximum IAP value is reached. In general, the duration of period II, where homogenous nucleation is suggested to predominate, decreases with increasing pH , which can be explained by significantly higher ACAR and rapidly increasing IAP with rise in pH . At $\text{pH} \geq 11.00$ the IAP threshold is reached immediately and the CaCO_3 nucleation and precipitation begins almost instantaneously after placing the bag containing the inner solution into the outer solution.

In the dominant precipitation period III of the experiments the IAP is high enough to stabilize CaCO_3 nuclei and crystal growth is predominating. The consumption of CO_3^{2-} in the outer solution by the overall precipitation of CaCO_3 (R_{CaCO_3}) exceeds the ACAR (see Fig. 23). This results - in combination with the decrease of Ca^{2+} concentration through CaCO_3 formation - in a decrease of the IAP (or of the saturation index) with respect to CaCO_3 until the end of the experiment (Figs. 8c to 10c). This evolution of IAP values as function of reaction time is valid for $\text{pH} \leq 10$. The subsequent precipitation period IV is characterized by the further growth of CaCO_3 crystals and the IAP decreases much slower. In contrast, at $\text{pH} \geq 11.00$ the IAP with respect to CaCO_3 increases during periods III and IV until the end of the experiment (Figs. 11c and 12c). This can be explained by lower R_{CaCO_3} values, which do not exceed the high ACAR at $\text{pH} \geq 11.00$ (see Fig. 23).

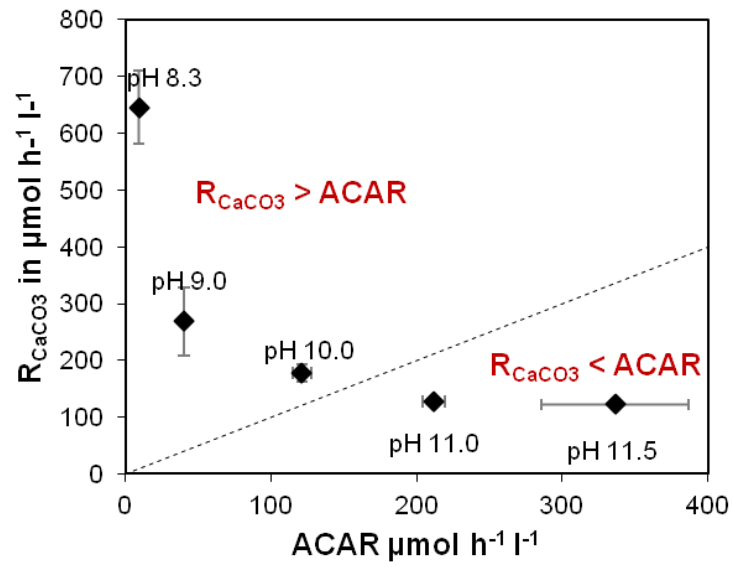


Fig. 23. Average aqueous carbonate accumulation rate, ACAR, versus the overall precipitation rate of CaCO₃, R_{CaCO₃}, from experiments (#1-10) in period III.

5.4 Precipitation rates of CaCO_3

The overall precipitation rates of CaCO_3 in the dominant precipitation period III are significantly higher at low versus high pH (Fig. 14a). The experimental study from Niedermayr et al. (2013) showed that at a given temperature, an increase in ACAR results in higher IAP_{fc} values, which is related to higher R_{CaCO_3} . The results of the present study show that higher vs. lower pH values are associated with higher ACAR and higher IAP_{fc} , but the corresponding R_{CaCO_3} values are lower. As seen in Fig. 24 the obtained ACAR and R_{CaCO_3} values from Niedermayr et al. (2013) show a positive correlation (open and grey diamonds), whereas the values from the present study are negative correlated (black diamonds).

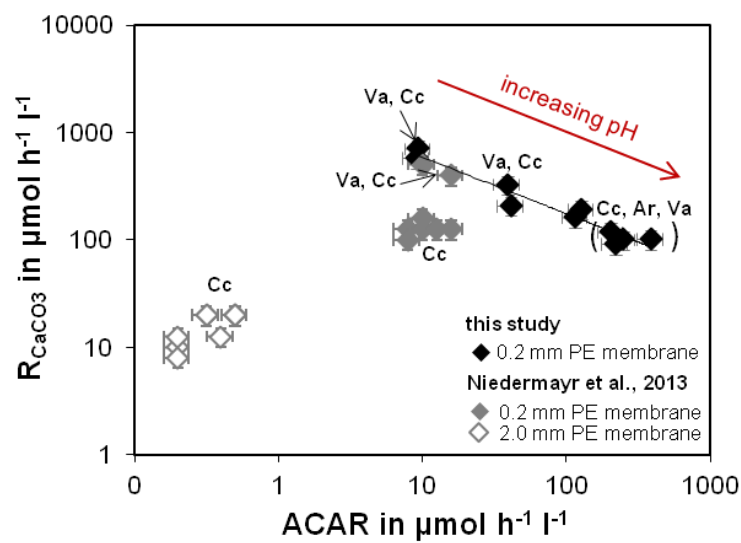


Fig. 24. Precipitation rates of CaCO_3 , R_{CaCO_3} , versus the aqueous carbonate accumulation rates, ACAR, of experiments (25°C) from the present study (#1-10) and from Niedermayr et al. (2013). (): experiments at $\text{pH} \geq 11$ (#4-5, #9-10), where $t_{\text{fc}} = 0.5$ h was assessed.

Niedermayr et al. (2013) observed that the precipitation rate of CaCO_3 increases in the order of calcite, aragonite and vaterite by keeping the supersaturation threshold of an individual CaCO_3 phase constant. Our R_{CaCO_3} values are based on consumed Ca^{2+} ions during the precipitation of the bulk CaCO_3 and comprise individual fractions of calcite, aragonite and vaterite (X_{Cc} , X_{Ar} and X_{Va} in Tab. 1). For instance, at pH 8.30, experiment #1 yield in the fractions of 43 and 57 wt. % for calcite and vaterite, respectively. At pH 9.00 the amount of calcite is only about 13 wt. % and vaterite occurs with 87 wt. % (experiment #2). Obviously, elevated amounts of vaterite occur at pH 9.00, which should result in an elevated overall precipitation rate according to Niedermayr et al. (2013). However, in the present study the obtained R_{CaCO_3} is significantly lower at pH 9.00 ($328 \mu\text{mol h}^{-1} \text{l}^{-1}$) compared to pH 8.30 (710

$\mu\text{mol h}^{-1} \text{ l}^{-1}$). These results suggest that in our experiments the pH has a much greater impact on the precipitation rate than the occurrence of distinct CaCO_3 polymorphs.

The decrease of the CaCO_3 precipitation rate at elevated pH of the present study (Fig. 14a) can be explained by considering the formation of hydrated CaCO_3 surface species and the effect of OH^- ions. Ruiz-Agudo et al. (2011) stated that at $\text{pH} < 8.5$ the calcite growth is mainly contributed by the incorporation of CaCO_3^0 at $>\text{CaHCO}_3^0$ surface sites. At $\text{pH} > 9.0$ the presence of OH^- facilitates the Ca^{2+} dehydration and its incorporation to $>\text{CaHCO}_3^0$ plays a more important role. The experimental study of Ruiz-Agudo et al. (2011) indicated for an increase of pH a decrease of concentrations of active growth sites, in particular $>\text{CaHCO}_3^0$, which reduces the overall calcite growth rate. Fig. 25 shows the modeled surface concentration of $>\text{CaHCO}_3^0$ (in $\mu\text{mol m}^{-2}$) for calcite versus pH (from Ruiz-Agudo et al., 2011). Although, the surface characteristics are different for distinct CaCO_3 polymorphs, the general relationship between surface complex formation of MeCO_3 minerals and pH is similar (Van Cappellen et al., 1993).

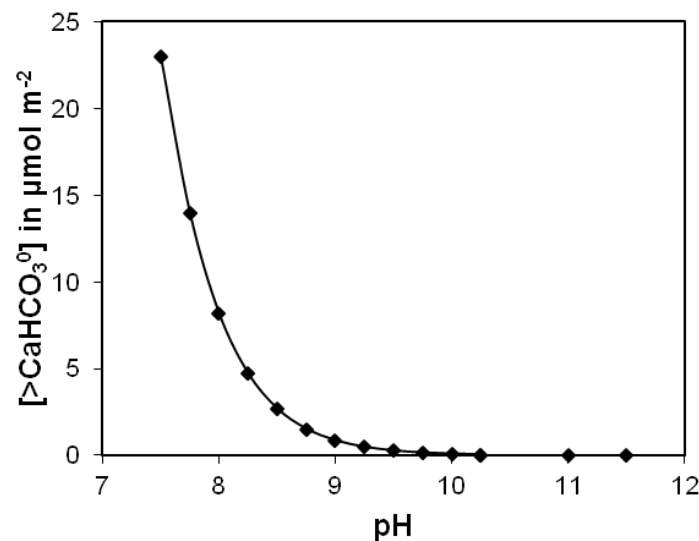


Fig. 25. PHEEQ C modeling of the concentration of $>\text{CaHCO}_3^0$ of a calcite cleavage surface versus pH (Ruiz-Agudo et al., 2011).

In Fig. 26 the obtained R_{CaCO_3} values from the dominant precipitation period III of the present study are plotted against the concentration of $>\text{CaHCO}_3^0$ obtained from Fig. 25. Obviously, elevated concentrations of $>\text{CaHCO}_3^0$ are related to higher R_{CaCO_3} values according to the equation

$$R_{\text{CaCO}_3} = 120 \cdot [>\text{CaHCO}_3^0] + 143.7 \quad (28)$$

Higher R_{CaCO_3} values at low versus high pH correlate with a general decrease of $[>\text{CaHCO}_3^0]$ at the CaCO_3 surface (exemplarily given for calcite in Fig. 26).

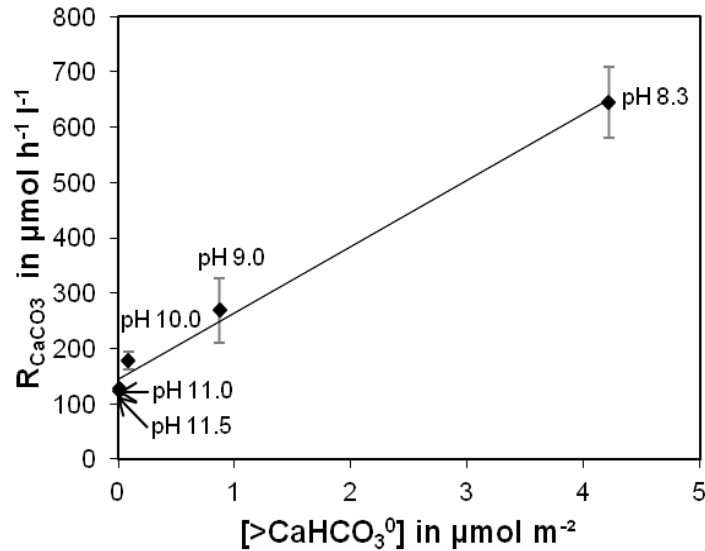


Fig. 26. Overall precipitation rates of CaCO_3 , R_{CaCO_3} , of sets 1 and 2, in the dominant precipitation period III from the present study versus the concentration of $>\text{CaHCO}_3^0$ (values are given for calcite from Ruiz-Agudo et al., 2011).

At $\text{pH} \leq 10.00$ the R_{CaCO_3} value exceeds the ACAR and the consumption of CO_3^{2-} is related to a decrease of the IAP (or saturation index) with respect to CaCO_3 until the end of the experiment. Consequently, the R_{CaCO_3} values are lowered down within period IV. As soon as the IAP decreases in experiments at $\text{pH} \leq 10.00$ and as soon as the IAP reaches a maximum value in experiments at $\text{pH} \geq 11.00$ the last precipitation period IV is characterized by similar R_{CaCO_3} values for all conducted experiments.

The combination of the aqueous CO_3^{2-} accumulation kinetic (elevated pH results in high ACAR) and the CaCO_3 precipitation kinetic (elevated pH results in low R_{CaCO_3}) yield in similar amounts of consumed $[\text{Ca}]$ of about 22 ± 4 mol% (in respect to initial Ca^{2+} concentrations) for all experiments by reaching the total experimental time of about 20 h (Fig. 14b).

5.5 CaCO₃ modifications

Experimental results by Niedermayr et al. (2013) clearly showed that the ACAR has a strong impact on the formation of individual CaCO₃ polymorphs. In our study, the ACAR strongly depends on the pH of the outer solution. Vaterite preferentially precipitated in experiments at pH ≤ 10.00, at low ACAR values. At pH ≥ 10.00, elevated ACAR values favors the formation of aragonite, where the maximal amount of aragonite was precipitated at pH 11.00. Calcite occurs at all pH values, but is formed at pH 11.50 in maximal proportions. Similar trends are reported by Tai et al. (1998), who investigated the polymorphism of CaCO₃ in a pH range between 8.00 and 12.50, using a constant-composition method (24 °C). They found that vaterite mainly precipitated in the pH range between 8.50 and 10.00, whereas aragonite showed a maximum at pH 11.00. The amount of calcite increased with rise in pH and it is a dominant product at pH > 12.00. Thus, the pH value of the solution has an important impact on the occurrence of calcite, aragonite and vaterite. However, the CaCO₃ polymorph formation mechanisms are complex and related to the huge number of factors such as temperature (Morse et al., 1997), reaction kinetics (Fernández-Díaz et al., 1996) and additives like Mg²⁺ (Niedermayr et al., 2013).

5.6 Coprecipitation of strontium with CaCO_3

The high proportion of aragonite in the precipitate at $\text{pH} \geq 10.00$ leads to high D_{Sr} values because of the preferential Sr^{2+} incorporation into the orthorhombic structure of aragonite. High D_{Sr} values are related to a strong decrease of $[\text{Sr}]/[\text{Ca}]$ ratio in the outer solution and a lower slope in Figs. 16c to 16e. The absence of aragonite at $\text{pH} \leq 9.00$ results in lower D_{Sr} values and higher slopes in Figs. 16a and 16b. The positive correlation of D_{Sr} with the relative amount of aragonite ($A_{\text{r,relative}}$) in the precipitate is shown in Fig. 27. The increase of $A_{\text{r,relative}}$ results in an increase of the D_{Sr} value.

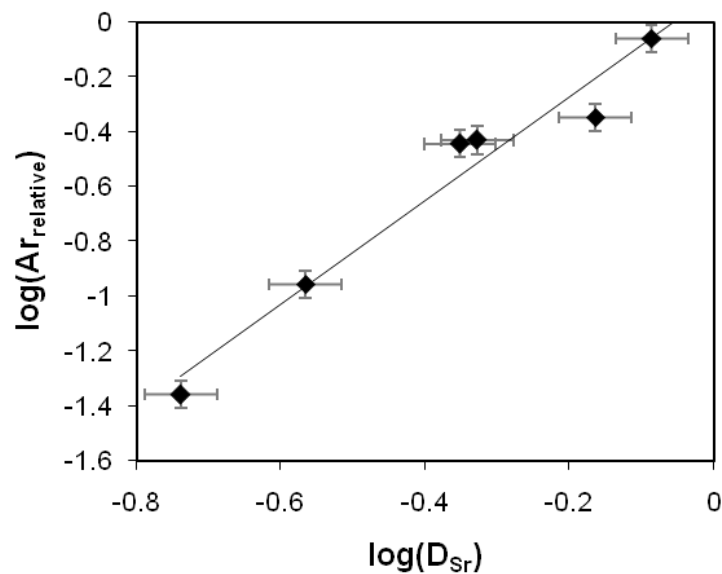


Fig. 27. Overall Sr distribution coefficient in CaCO_3 , D_{Sr} , versus the relative amount of aragonite in the precipitate (#3-5, #8-10).

Nearly constant D_{Sr} values during an experimental run (Figs. 16a to 16e) indicate almost uniform CaCO_3 polymorph fractions during the ongoing precipitation in individual experiments, especially in respect to the aragonite content vs. calcite and vaterite. Thus it can be reasonable assumed that the CaCO_3 polymorphs nucleates depending on the individual initial conditions and growth occur without significant changes in polymorph proportions. This is conform with the results from Niedermayr et al. (2013) for analyzing the occurrence of CaCO_3 precipitates at distinct formation intervals using an analogous experimental approach.

Periods III and IV of individual experiments yield in different R_{CaCO_3} values, especially at $\text{pH} \leq 10.00$, but the obtained D_{Sr} values are nearly constant during the whole experiment. Even highest changes of the R_{CaCO_3} values during the experiment #1 ($\text{pH} 8.30$) from 710 to $91 \mu\text{m h}^{-1} \text{ l}^{-1}$ in periods IV and III, respectively, have no significant impact on the overall D_{Sr} value

($D_{Sr} = 0.160 \pm 0.003$ in Fig. 16a). This is in general accordance with the low D_{Sr} variability at elevated precipitation rates for instance with respect to calcite, where the above changes of the R_{CaCO_3} values yield in D_{Sr} variability of only about ± 0.03 (see Tang et al., 2008 for 25°C).

5.7 Coprecipitation of boron with CaCO_3

It is assumed that B(OH)_4^- is the aqueous species, which is preferentially incorporated into calcium carbonates (Hemming and Hanson, 1992) and thus the B versus Ca concentration of CaCO_3 precipitates should increase with increasing pH. Our results show that the measured B/Ca ratio of the received precipitates increases from pH 8.30 to 10.00 and at $\text{pH} \geq 10.00$ the ratio remains almost constant (Fig. 17). In Fig. 28 the B/Ca ratio of the CaCO_3 precipitates were plotted against the modeled activity of B(OH)_4^- of the outer solution (black squares). An increase in pH is related to higher B(OH)_4^- activities and causes higher boron concentrations of the precipitates. As at $\text{pH} > 10.00$ almost all dissolved boron is essentially referred to B(OH)_4^- , the B/Ca ratio in CaCO_3 precipitates may be useful as proxy in the pH range between 8.30 and 10.00 (see also Zeebe et al., 2001 and references therein).

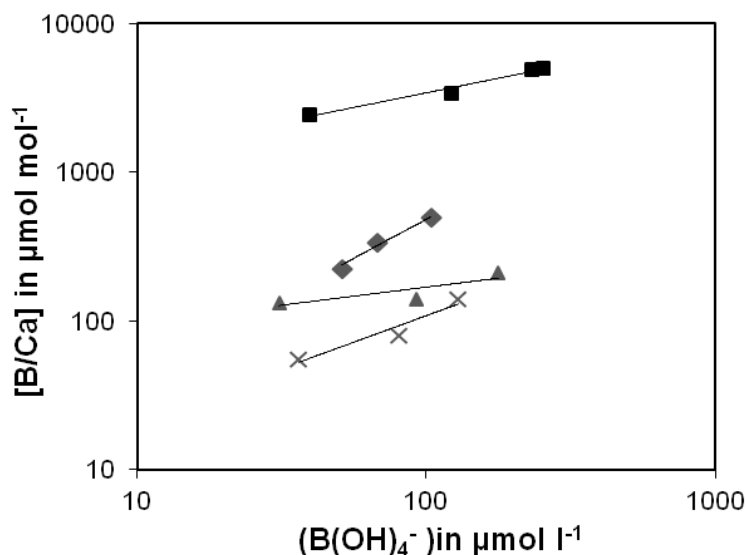


Fig. 28. Measured B/Ca ratio of the CaCO_3 precipitates versus the activity of B(OH)_4^- in the outer solution from the present study (#6-8, #10), from Hemming and Hanson, 1992 (high-Mg calcite and aragonite from modern sea water), from Sanyal et al., 2000 (inorganic calcite precipitated in artificial seawater) and from Allen et al., 2012 (calcite of planktic foraminifers of culture experiments in seawater).

The positive correlation of B/Ca with the activity of B(OH)_4^- is also shown by studies from Hemming and Hanson (1992), Sanyal et al. (2000) and Allen et al. (2012) with respect to tested modern carbonates, inorganic precipitated calcite in artificial seawater and cultured planktic foraminifers, respectively. However, the B/Ca values from the present study are considerably higher compared to the values from the above mentioned studies. This could be explained by extraordinary high R_{CaCO_3} values in experiments from the present study, which

may result in a preferential incorporation of $\text{B}(\text{OH})_4^-$ into the bulk CaCO_3 (kinetic fractionation). As seen in Fig. 29 elevated R_{CaCO_3} values (at lower pH conditions) correlate with higher distribution coefficient with respect to B/Ca and $\text{B}(\text{OH})_4^-$. Thus, the effect of the precipitation rate of CaCO_3 should be considered in the further development of B/Ca as proxy for pH.

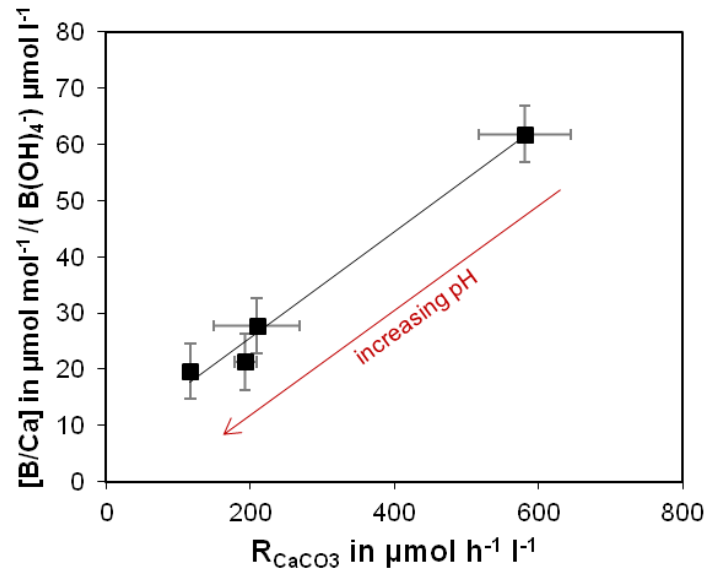


Fig. 29. Overall precipitation rates of CaCO_3 , R_{CaCO_3} , versus the quotient of the molar B/Ca in the CaCO_3 precipitate and the activity of $\text{B}(\text{OH})_4^-$ in the outer solution (#6-8, #10).

5.8 Oxygen isotopes

The obtained $\delta^{18}\text{O}$ values of the initial and final outer solutions (-39.0 ± 0.1 ‰ (VPDB)) clearly indicates constant isotopic composition of the used water and no evaporation during the experimental time. The analysed isotopic composition of the received bulk CaCO_3 yields in isotopically lighter CaCO_3 at elevated pH (Fig. 18). At pH 8.30 the $^{18}\text{O}/^{16}\text{O}$ fractionation between CaCO_3 and H_2O is closely related to isotope exchange equilibrium conditions in respect to calcite at 25°C (this study: $1000 \cdot \ln\alpha_{\text{CaCO}_3\text{-H}_2\text{O}} = 29.2$ ‰ (see data in Tab. 1); Kim and O'Neil, 1997, for calcite at 25°C : $1000 \cdot \ln\alpha_{\text{calcite-H}_2\text{O}} = 28.1$ ‰; Dietzel et al., 2009, for calcite at 25°C and slowest R_{CaCO_3} value: $1000 \cdot \ln\alpha_{\text{calcite-H}_2\text{O}} = 30.6$ ‰; Tarutani et al., 1969, for aragonite at 25°C : $1000 \cdot \ln\alpha_{\text{aragonite-H}_2\text{O}} = 28.7$ ‰). In strong alkaline solutions CO_2 reacts preferentially with OH^- (hydroxylation) to HCO_3^- (reaction 25), which dissociates to CO_3^{2-} . During the hydroxylation of CO_2 the CO_2 reacts with OH^- without isotopically equilibration with the H_2O (Dietzel, 2000 and references therein). Thus, isotope oxygen non-equilibrium of CO_2 with water is valid as the hydroxylation dominates over hydration of CO_2 and instantaneous dissociation of HCO_3^- results in isotopically lighter CO_3^{2-} (compared to equilibrium conditions), which is subsequently fixed in the CaCO_3 (e.g. at pH 11.50 our measured $1000 \cdot \ln\alpha_{\text{CaCO}_3\text{-H}_2\text{O}}$ value is 12.1 ± 0.1 ‰), which is based on a kinetically driven isotope fractionation due to CO_2 hydroxylation of about 18 ‰ (Dietzel, 2000). Thus, in the present study the $\delta^{18}\text{O}$ value of CaCO_3 precipitates can be used as a proxy for pH during its formation, where isotopically lighter CaCO_3 is formed at elevated pH due to CO_2 hydroxylation (Fig. 18).

6. SUMMARY AND CONCLUSION

In the present study CaCO_3 precipitation experiments were carried out in the pH range from 8.30 to 11.50 by using a CO_2 -diffusion technique. The aim of this study was to investigate the effect of pH on the aqueous carbonate accumulation and the CaCO_3 precipitation kinetic as well as on the formation of distinct CaCO_3 polymorphs. Furthermore, the coprecipitation of Sr^{2+} and B with CaCO_3 and the isotopic oxygen composition of the CaCO_3 precipitates were studied.

The used technique is based on the diffusion of CO_2 through a polyethylene membrane from an inner into an outer solution, containing 10 mM of CaCl_2 , 0.1 mM SrCl_2 and 0.4 mM NaBO_2 , where the latter has been omitted in the first of two experimental sets (25°C). The pH of the outer solution was kept constant by adding 0.5 M NaOH solution. When an IAP threshold with respect to CaCO_3 is reached calcium carbonate is formed in the outer solution. The evolution of the NaOH titration curve and the measured $[\text{Ca}^{2+}]$ reflect parameters like the uptake rate of CO_2 in the outer solution ($UT_{\text{CO}_2\text{av}}$), the aqueous carbonate accumulation rate (ACAR) and the overall precipitation rate of CaCO_3 (R_{CaCO_3}).

The $UT_{\text{CO}_2\text{av}}$ of the outer solution increases with rise in pH as the CO_2 partial pressure gradient between the inner and the outer solution increases. The continuous uptake and dissociation of CO_2 result in the accumulation of CO_3^{2-} ions in the outer solution. The ACAR is higher at elevated pH, depending on the P_{CO_2} gradient between the inner and the outer solution, the dominance of the CO_2 hydroxylation and the $[\text{CO}_3^{2-}]/[\text{DIC}]$ ratios. In strongly alkaline solutions the elevated ACAR causes rapidly increasing IAP for CaCO_3 and the time of first net CaCO_3 nucleation (t_{fc}) is reached earlier. At $\text{pH} \geq 11.00$ the CaCO_3 nucleation and precipitation begins instantaneously after starting the experiment.

In contrast to the ACAR, the R_{CaCO_3} is significantly lower at high versus low pH, if once an IAP threshold is reached in the outer solution. The decrease of the R_{CaCO_3} with rise in pH can be explained by the general decrease of the surface concentration of $>\text{CaHCO}_3^0$ at CaCO_3 surfaces at elevated pH.

Thus, high pH values of the outer solution yield in elevated ACAR and low R_{CaCO_3} , whereas low ACAR and high R_{CaCO_3} are related to low pH values. The combination of the aqueous

CO_3^{2-} accumulation kinetic and the precipitation kinetic of CaCO_3 results in similar amounts of consumed [Ca] (equivalent to the amount of precipitated CaCO_3) of about 22 ± 4 mol % in respect to initially dissolved calcium for all experiments by reaching the total experimental time of about 20 h.

(Micro)Raman and XRD pattern as well as SEM images clearly reveal the formation of calcite and vaterite in all experiments. The formation of individual CaCO_3 polymorphs strongly depends on the pH value of the outer solution. Vaterite dominates at $\text{pH} \leq 10.00$, whereas calcite shows a maximum at pH 11.50. At $\text{pH} \geq 10.00$ aragonite additionally occurs, especially at pH 11.00. The present of boron shows no clear impact on the occurrence of CaCO_3 polymorphs. However, further experiments are required to clarify the detailed influence of boron of CaCO_3 polymorph formation.

The high proportion of aragonite in the precipitates at $\text{pH} \geq 10.00$ leads to high overall distribution coefficients for Sr between the aqueous solution and bulk CaCO_3 (D_{Sr}) caused by the preferential Sr incorporation into the aragonite structure compared to calcite and vaterite. Nearly constant D_{Sr} values during the experimental runs indicate a rather uniform individual CaCO_3 polymorph proportions during the ongoing precipitation (see Fig. 16). The results show that the D_{Sr} value is predetermined by the proportion of precipitated aragonite in the bulk CaCO_3 and is not significantly affected by the changes in precipitation rates in our experiments.

The B/Ca ratio of the analyzed CaCO_3 precipitates increases with rise in pH of the outer solution due to the increase of the activity of the $\text{B}(\text{OH})_4^-$, which is assumed to be incorporated into calcium carbonate. At $\text{pH} \geq 10.00$ a limit in the activity of $\text{B}(\text{OH})_4^-$ for the respective B concentration of the solution as well as in the B/Ca ratio of the precipitate is reached. Thus, the coprecipitation of B with CaCO_3 can be used as a proxy for the pH value of the solution at $\text{pH} \leq 10.00$. However, in comparison with literature data an impact of the CaCO_3 precipitation rate on boron coprecipitation with CaCO_3 has been considered.

The oxygen isotopic compositions of the CaCO_3 precipitates show that isotopically lighter CaCO_3 is formed at elevated pH compared to lower pH conditions. The isotopic fractionation of ^{18}O and ^{16}O between water and CaCO_3 is determined by the equilibrium (e.g. in our experiments at pH 8.30) or non-equilibrium (e.g. at pH 11.50) at low versus high pH,

respectively. Thus, the oxygen isotopic composition of CaCO_3 can be used as proxy for pH based on kinetically driven isotope fractionation.

The results of the present study can be applied to man-made and natural environments, where precipitation of CaCO_3 occurs in highly alkaline solutions. The results indicate that for uptake of gaseous CO_2 in an alkaline solution, the pH is not a decisive factor to quantify the amounts of CaCO_3 precipitation throughout reaction time. The overall precipitation rate of CaCO_3 is negatively correlated with the pH value of the aqueous solution. In contrast, the uptake rate of CO_2 and the aqueous carbonate accumulation rate in the aqueous solution increase at elevated pH value. Thus, the combined effect of the aqueous carbonate accumulation rate and the precipitation rate of CaCO_3 controls the formation and quantification of CaCO_3 . Nevertheless, it must be pointed out that the nucleation and precipitation of CaCO_3 starts earlier at elevated pH conditions (lower t_{fc} values) due to the elevated aqueous accumulation of CO_3^{2-} .

Our results confirmed that the ratio of B/Ca as well as the oxygen isotopic composition of CaCO_3 precipitates depends on the pH value of the solution. These proxies can be useful for the reconstruction of pH values from CaCO_3 precipitates in natural and man-made alkaline environments. However, kinetic aspects for the coprecipitation of B with CaCO_3 and in respect to CO_2 hydroxylation have to be considered. In contrast, Sr incorporation into CaCO_3 precipitates is highly stimulated by aragonite formation in strong alkaline solutions, whereas the impact of precipitation rate on D_{Sr} can be neglected.

7. REFERENCES

- Allen, K.A., Hönisch, B., Eggins, S.M., Rosenthal, Y., 2012. Environmental controls on B/Ca in calcite tests of the tropical planktic foraminifer species *Globigerinoides ruber* and *Globigerinoides sacculifer*. *Earth and Planetary Science Letters* **351-352**, 270-280.
- Appelo, C. A. J., Postma, D., 2010. *Geochemistry, groundwater and pollution*. Balkema, Rotterdam, 649 p.
- Back, M., Bauer, M., Stanjek, H., Peiffer, S., 2011. Sequestration of CO₂ after reaction with alkaline earth metaloxides CaO and MgO. *Applied Geochemistry* **26**, 1097-1107.
- Berndt, M.E., Seyfried, W.E., 1999. Rates of aragonite conversion to calcite in dilute aqueous fluids at 50 to 100°C: Experimental calibration using Ca-isotope attenuation. *Geochimica et Cosmochimica Acta* **63**, 373–381.
- Böttcher, M., Dietzel, M., 2010. Metal-ion partitioning during low-temperature precipitation and dissolution of anhydrous carbonates and sulfates. In: Ion partitioning in low temperature aqueous systems (Eds.; Prieto M., Stoll H.). *EMU Notes in Mineralogy* **10**, 139-187.
- Clark, I.D., Fontes, J.-C., Fritz, P., 1992. Stable isotope disequilibria in travertine from high pH waters: Laboratory investigations and field observations from Oman. *Geochimica et Cosmochimica Acta* **56**, 2041-2050.
- De Villiers, S., Shen, G.T., Nelson, B.K., 1994. The Sr/Ca-temperature relationship in coralline aragonite: Influence of variability in (Sr/Ca)_{seawater} and skeletal growth parameters. *Geochimica et Cosmochimica Acta* **58**, 197-208.
- Dietzel, M., 2011. Carbonates. In: *Encyclopedia of Geobiology*. (eds.: Reitner, J., Thiel, V.). Springer, Berlin, 261-266.
- Dietzel, M., 2000. Messungen der stabilen Isotope des Kohlenstoffs an Kalk-Versinterungen von Beton. *Cement-Lime-Gypsum-International* **53** (9), 544-548.
- Dietzel, M., Usdowski, E., Hoefs, J., 1992. Chemical and ¹³C/¹²C- and ¹⁸O/¹⁶O-isotope evolution of alkaline drainage waters and the precipitation of calcite. *Applied Geochemistry* **7**, 177-184.
- Dietzel, M., Tang, T., Leis, A., Köhler, S.J., 2009. Oxygen isotopic fractionation during inorganic calcite precipitation – Effects of temperature, precipitation rate and pH. *Chemical Geology* **268**, 107-115.
- Erez, J., Luz, B., 1983. Experimental paleotemperature equation for planktonic foraminifera. *Geochimica et Cosmochimica Acta* **47**, 1025-1031.
- Fernández-Díaz, L., Putnis, A., Prieto, M., Putnis, C. V., 1996. The role of magnesium in the crystallization of calcite and aragonite in a porous medium. *Journal of Sedimentary Research* **66**, 482-481.

- Gaetani, G.A., Cohen, A.L., 2006. Element partitioning during precipitation of aragonite from seawater: A framework for understanding paleoproxies. *Geochimica et Cosmochimica Acta* **70**, 4617–4634.
- Gauldie, R.W., Sharma, S.K., Volk, E., 1997. Micro-Raman Spectral Study of Vaterite and Aragonite Otoliths of the Coho Salmon, *Oncorhynchus kisutch*. *Camp, Biochem. Physiol.* **118A**, 753-757.
- Gosh, P., Adkins, J., Affek, H., Balta, B., Guo, W., Schauble, E.A., Schrag, Dan., Eiler, J.M., 2006. ^{13}C – ^{18}O bonds in carbonate minerals: A new kind of paleothermometer. *Geochimica et Cosmochimica Acta* **70**, 1439-1456.
- Gussone, N., Nehrke, G., Teichert, B., 2011. Calcium isotope fractionation in ikaite and vaterite. *Chemical Geology* **285**, 194–202.
- Hemming, N.G., Hanson, G.N., 1992. Boron isotopic composition and concentration in modern marine carbonates. *Geochimica et Cosmochimica Acta* **56**, 537-543.
- Hoefs, J., 2009. *Stable isotope geochemistry*. Springer, Heidelberg, 285 p.
- Hover, V.C., Walter, Lynn, M., Peacor, D.R., 2001. Early marine diagenesis of biogenic aragonite and Mg-calcite: new constraints from high-resolution STEM and AEM analyses of modern platform carbonates. *Chemical Geology* **175**, 221-248.
- Huang, Y., Fairchild, I. J., Borsato, A., Frisia, S., Cassidy, N. J., McDermott, F., Hawkesworth, C. J., 2001. Seasonal variations in Sr, Mg and P in modern speleothems (Grotta di Ernesto, Italy). *Chemical Geology* **175**, 429-448.
- Kim, S.-T., O'Neil, J.R., 1997. Equilibrium and nonequilibrium oxygen isotope effects in synthetic carbonates, *Geochimica et Cosmochimica Acta*, **61**, 3461–3475.
- Kontoyannis, C. G., Vagenas, N. V., 2000. Calcium carbonate phase analysis using XRD and FT-Raman spectroscopy. *Analyst* **125**, 251-255.
- Lorens, R. B., 1981. Sr, Cd, Mn and Co distribution coefficients in calcite as a function of calcite precipitation rate. *Geochimica et Cosmochimica Acta* **45**, 553-561.
- Ma, Y., Berland, S., Andrieu, J.P., Feng, Q., Bédouet, L., 2013. What is the difference in organic matrix of aragonite vs. vaterite polymorph in natural shell and pearl? Study of the pearl-forming freshwater bivalve mollusc *Hyriopsis cumingii*. *Materials Science and Engineering C* **33**, 1521–1529.
- Mackenzie, F.T., Morse, J.W., 1992. Sedimentary carbonates through Phanerozoic time. *Geochimica et Cosmochimica Acta* **56**, 3281-3295.
- Montes-Hernandez, G., Chiriach, R. Toche, F., Renard, F., 2012. Gas-solid carbonation of $\text{Ca}(\text{OH})_2$ and CaO particles under non-isothermal and isothermal conditions by using a thermogravimetric analyzer: Implications for CO_2 capture. *International Journal of Greenhouse Gas Control* **11**, 172-180.

- Morse, J.W., Arvidson, R.S., 2002. The dissolution kinetics of major sedimentary carbonate minerals. *Earth-Science Reviews* **58**, 51–84.
- Morse, J.W., Mackenzie, F.T., 1990. Geochemistry of sedimentary carbonates. *Developments in Sedimentology* **48**, 707.
- Morse, J.W., Wang, Q., Tsio, M.Y., 1997. Influences of temperature and Mg:Ca ratio on CaCO₃ precipitates from seawater. *Geology* **25**, 85-87.
- Niedermayr, A., Köhler, S.J. Dietzel, M., 2013. Impacts of aqueous carbonate accumulation rate, magnesium and polyaspartic acid on calcium carbonate formation (6-40°C). *Chemical Geology* **340**, 105-120.
- O'Neil, J.R., 1977. Stable isotopes in mineralogy. *Phys Chem Miner* **2**, 105-123
- Orr, J.C., Caldeira, K., Fabry, V., Gattuso, J.-P., Haugan, P., Lehodey, P., Pantoja, S., Pörtner, H.-O., Riebesell, U., Trull, T., and others, 2009. Research priorities for understanding ocean acidification: Summary from the Second Symposium on the Ocean in a High-CO₂ World. *Oceanography* **22**(4),182–189.
- Park, S.Y., Choi, W.S., 2004. Effects of operating factors on the particle size distribution and particle shape of synthesized precipitated CaCO₃: effect of reaction temperature, blowing rate of CO₂ gas and initial slurry concentration of Ca(OH)₂ on reaction completion time. *Advanced Powder Technology* **15**, 1-12.
- Plummer, L.N., Busenberg, E., 1982. Solubilities of calcite, aragonite and vaterite in CO₂-H₂O solutions between 0 and 90°C, and an evaluation of the aqueous model for the system CaCO₃-CO₂-H₂O. *Geochimica et Cosmochimica Acta* **46**, 1011-1040.
- Reeder, R.J., 1990. Carbonates: mineralogy and chemistry. *Reviews in Mineralogy*, **11**, 399 p.
- Rinder, T., Dietzel, M., Leis, A., 2013. Calcium Carbonate Scaling under Alkaline Conditions – Case Studies and Hydrochemical Modelling. *Applied Geochemistry*, in press.
- Ruiz-Agudo, E., Putnis, C.V., Kowacz, M. Ortega-Huertas, M., Putnis, A., 2012. Boron incorporation into calcite during growth: Implications for the use of boron in carbonates as a pH proxy. *Earth and Planetary Science Letters* **345-348**, 9-17.
- Ruiz-Agudo, E., Putnis, C.V., Rodriguez-Navarro, C., Putnis, A., 2011. Effect of pH on calcite growth at constant $\alpha_{\text{Ca}^{2+}}/\alpha_{\text{CO}_3^{2-}}$ - ratio and supersaturation. *Geochimica et Cosmochimica Acta* **75**, 284-296.
- Sanyal, A., Nugent, M., Reeder, R.J., Bijma, J., 2000. *Geochimica et Cosmochimica Acta* **64**, 1551-1555
- Spötl, C., Vennemann, T.W., 2003. Continuous-flow isotope mass spectrometric analysis of carbonate minerals. *Rapid Communications in Mass Spectrometry* **17**, 1004-1006.
- Stumm, W., Morgan, J. J., 1996. *Aquatic Chemistry: chemical equilibria and rates in natural waters*. Wiley-Interscience, New York, 1022 p.

- Tai, C. Y., Chen, F.B., 1998, Polymorphism of CaCO₃, precipitated in a constant-composition environment. *AIChE J.* **44**, 1790–1798.
- Tang, J., Köhler, S.J., Dietzel, M., 2008. Sr²⁺/Ca²⁺ and ⁴⁴Ca/⁴⁰Ca fractionation during inorganic calcite formation: I. Sr Incorporation. *Geochimica et Cosmochimica Acta* **72**, 3718-3732.
- Tarutani, T., Clayton, R. N., Mayeda, T. K., 1969. The effect of polymorphism and magnesium substitution on oxygen isotope fractionation between calcium carbonate and water. *Geochimica et Cosmochimica Acta* **33**, 987–996
- Urey, H. C., 1947. The thermodynamic properties of isotopic substances. *J. Chem. Soc.*, 562.
- Usdowski, E., 1982. Reactions and Equilibria in the Systems CO₂-H₂O and CaCO₃-CO₂-H₂O (0°-50°C). A Review. *N. Jb. Miner. Abh.* **144**, 148-171.
- Van Cappellen, P., Charlet, L., Stumm, W., Wersin, P., 1993. A surface complexation model of the carbonate mineral-aqueous solution interface. *Geochimica et Cosmochimica Acta* **57**, 3505-3518.
- Zeebe, R. E., Wolf-Gladrow, D., 2001. CO₂ in Seawater: Equilibrium, Kinetics, Isotopes. *Equilibrium, Kinetics, Isotopes* **65**, Elsevier Science.

8. APPENDIX

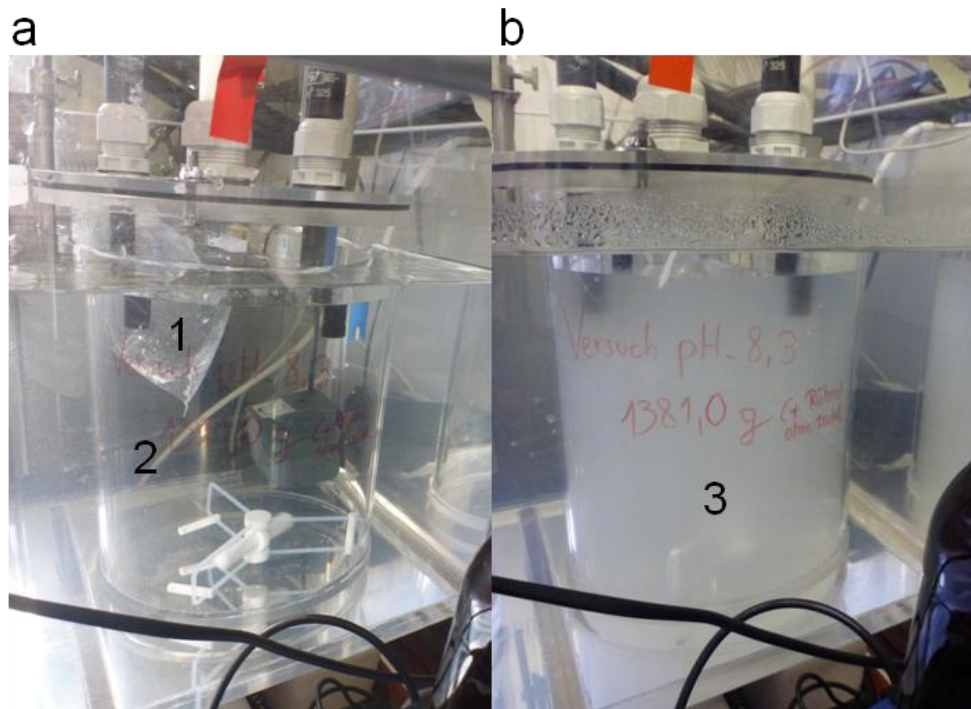


Fig. A1. Images of the experiment at pH 8.30 (#1), where (a) CO_2 diffuses from the inner (1) into the outer (2) solution and (b) CaCO_3 was formed in the outer solution (3).

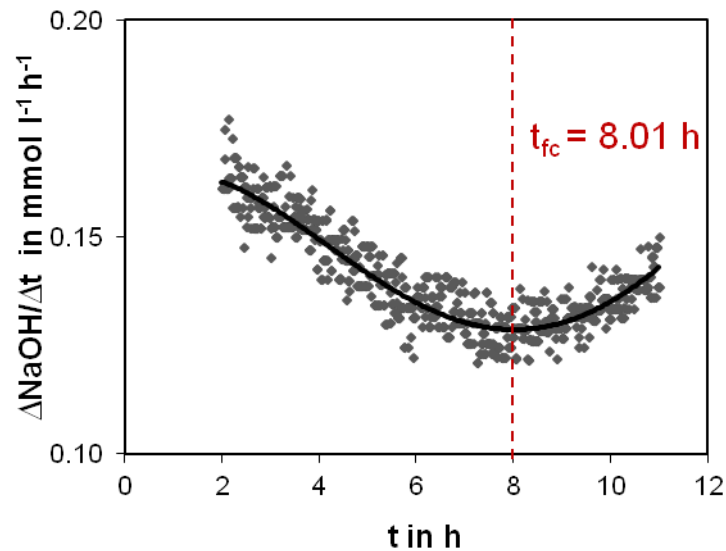


Fig. A2. First derivation of the NaOH titration curve at pH 8.30 (#1). t_{fc} denotes the time of first net nucleation of CaCO_3 and is given by the minimum of the polynomial regression function ($\Delta\text{NaOH}/\Delta t = -1.39 \cdot 10^{-5} t^4 + 4.80 \cdot 10^{-4} t^3 - 4.54 \cdot 10^{-3} t^2 + 8.84 \cdot 10^{-3} t + 0.16$ in this case) obtained by least square method (black solid curve; $R = 0.87$). The t_{fc} value (in this case: 8.01 h) was calculated by zeroize the derivation of the respective polynomial regression function.

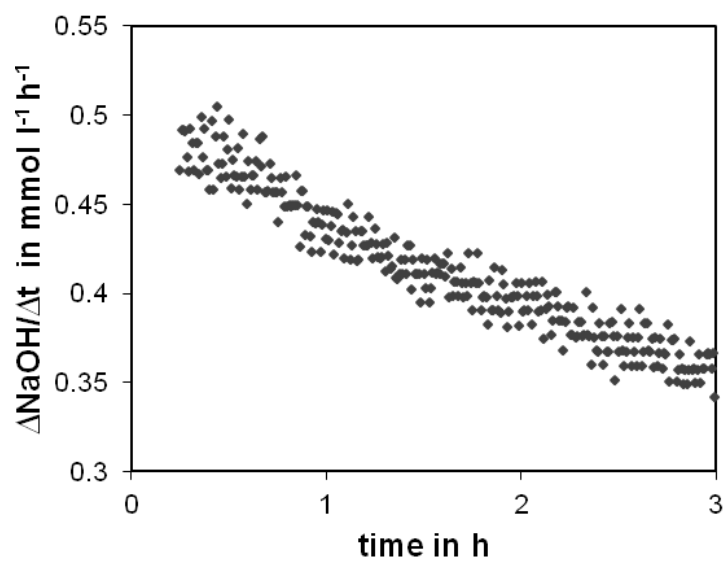


Fig. A2. First derivation of the resulted NaOH titration curve at pH 11.00 (#9).